Zr, Hf and REE distribution in river water under different ionic strength conditions

P. Censi, F. Sposito, C. Inguaggiato, P. Zuddas, S. Inguaggiato, M. Venturi

Zr, Hf AND REE DISTRIBUTION IN RIVER WATER UNDER DIFFERENT IONIC STRENGTH CONDITIONS

Censi P.[1*], Sposito F.[1,2], Inguaggiato C.[3], Zuddas P. [4], Inguaggiato S. [2], Venturi M.[5]

[1]Department of Earth and Marine Sciences, University of Palermo, Via Archirafi, 36 - 90123 Palermo, Italy.

[2] Istituto Nazionale di Geofisica e Vulcanologia, Sezione di Palermo, Via U. La Malfa, 153, 90146 Palermo, Italy.

[3] Departamento de Geología, Centro de Investigación Científica y de Educación Superior de Ensenada, Carretera Tijuana-Ensenada No. 3918, Zona Playitas, Ensenada, Baja California, C.P. 22860, Mexico.

[4] Sorbonne Universités, UPMC Univ. Paris 06, CNRS ISTEP, 4 place Jussieu 75005 Paris, France

[5] SIDERCEM S.R.L., Via L. Grassi, 7, 93100 Caltanissetta, Italy

* Corresponding Author paolo.censi@unipa.it

Abstract

The Platani River flowing in south-central Sicily, interacting with evaporite rocks, generates a wide range of ionic strength in the water catchment from 0.1 to 5.0 mol kg^{-1}. We sampled 38 river sites and analysed the composition for the dissolved fraction filtered through 0.45 μm, the truly dissolved fraction obtained through ultrafiltration (10 KDa) and the relative included colloidal fraction.

This study was focused on the recognition of Zr, Hf and REE behaviour under changing ionic strength conditions, since this is one of parameters responsible for colloid stability in natural waters.

In turn, this phenomenon leads to REE release from the colloidal fraction and their scavenging onto surfaces of suspended particles or sediment, or their complexation with dissolved ligands.

Our results indicated that in both dissolved and ultra-filtrated fractions REE increases either in the middle (Sm – Dy) or in the heavier (Ho – Lu) part of the PAAS-normalised distribution, while the Zr/Hf ratio value ranges from sub-chondritic to super-chondritic.

Scanning Electron Microscopic and Energy Dispersive X-ray Spectrometric (SEM-EDS) analyses and dissolved Mg, Al and Fe concentrations suggested that the studied colloids consist of aggregations of Al-oxyhydroxides, carbonate nanoparticles and clays where organic traces were not found. The studied colloids showed greater affinity with dissolved Zr than Hf determining Zr/Hf values larger than the chondritic values. The largest Zr/Hf values were found in colloidal fractions from waters with ionic strength larger than 0.6 mol kg^{-1}. These Zr/Hf values up to 280 (w/w) are provided by the faster removal of Hf relative to Zr from coagulating colloids and its preferential scavenging onto authigenic Fe-oxyhydroxides in bottom sediment. Further studies are needed to clarify is this suggested process can represent a suitable starting point for the Zr-Hf decoupling observed in seawater.

1. INTRODUCTION

Elements' transport from continent to seawater represents the main part of their exogenous cycle. Rare Earth Elements (REE) transport was investigated in a large number of scientific studies throughout the last 40 years (Elderfield and Greaves, 1982; Elderfield, 1988; Elderfield et al., 1990). These studies highlighted some REE characteristics occurring during aqueous processes including the large REE affinity towards solid surfaces and the related tendency of these elements to partition along the REE series. Accordingly, REE removal from the dissolved phase during reactions between suspended solids and colloids is one of the most common processes occurring in natural waters (Goldstein and Jacobsen, 1988; Sholkovitz and Elderfield, 1988; Elderfield et al., 1990; Sholkovitz et

al., 1994; Sholkovitz, 1992; 1995; Lawrence and Kamber, 2006; Rousseau et al., 2015; Merschel et al., 2017).

This sensitivity towards surfaces of different natures during interface processes was also recognised in natural waters for Zr and Hf (Schmidt et al., 2014; Inguaggiato et al., 2015; 2016; Censi et al., 2015; 2017). This sensitivity determined the decoupling of these elements that rum relative to their strong geochemical coherence evidenced during the crystallisation of rock-forming minerals (Bau, 1996).

Studies focused on the REE distribution in rivers showed the importance of estuaries as areas where the largest difference between geochemical behaviour of these elements in continental and seawater was emphasised throughout interface processes. The same effort for Zr and Hf consisted of some studies in rivers (Godfrey et al., 2008; Pokrovsky et al., 2010; 2014) and seawater (McKlivey and Orians, 1993; 1998; Godfrey et al., 1996; Firdaus et al., 2008; 2011; Frank, 2011).

REE studies demonstrated that the transport of metal ions occurs in colloids from continental waters (Sholkovitz, 1993; 1995; Lawrence and Kamber, 2006; Cidu and Frau, 2009; Cidu et al., 2013; Tepe and Bau, 2014; Johannesson et al., 2017; Merschel et al., 2017 and references therein). Accordingly, changes of ionic strength in estuaries were demonstrated to play a key role in determining the REE partitioning among dissolved phase, suspended particles and sediments and then influencing the REE transport from continents to the sea (Sholkovitz, 1995 and references therein; Elbaz-Poulichet and Dupuy, 1999; Sholkovitz and Szymczak, 2000; Nozaki et al., 2000; Hannigan and Sholkovitz, 2001; Barroux et al., 2006; Censi et al., 2007; 2010; Kulaksiz and Bau, 2007; 2011; Godfrey et al., 2008; Johannesson et al., 2017). On the other hand, the mixing of water masses and the regime of coastal currents can disturb the geochemical REE effect simply due to the contribution of ionic strength in estuaries.

The above-mentioned examples addressed to the Zr-Hf distribution in natural waters highlighted the large difference between the geochemical coherence of these twin elements in rocks and partially in

continental waters compared to the strong fractionation reported in seawater. The extent of this difference suggested several possible explanations of this finding, such as the incongruent weathering of zircon bearing rocks, Zr-Hf hydrothermal input in seawater, or Zr-Hf involvement in the biogeochemical cycles along the water column (Bau and Koschinsky, 2006; Frank, 2011).

In this study, our objective was to determine whether Zr-Hf decoupling under the effect of ionic strength may represent the starting point of large observed differences in Zr-Hf fractionation occurring in seawater relative to continental water. In turn, changes of ionic strength in waters could influence the Zr/Hf and REE signature of authigenic minerals and sediment fraction (Inguaggiato et al., 2018; Zuddas et al., 2018). In order to investigate this item, we have to investigate how aqueous Zr, Hf and REE distribution can react to severe changes of ionic strength along a small river far from its estuary. In the studied waters, the limited pH and Eh changes observed should have lower effects than the variation of ionic strength on the distribution of Zr, Hf and REE among colloids, truly dissolved fractions and river sediment. The location of the selected Platani river catchment is South-Central Sicily, where some of the largest Messinian evaporite deposits crop out in the Mediterranean (Rouchy and Caruso, 2006). The weathering of these deposits drives the high salt content of river waters, determining the required change of ionic strength spanning between 0.11 and 5.15 mol kg^{-1}. The size of the selected river and the turbulence of its waters causes the resuspension of the finest sediment fraction that in turn represents the main component of the suspended river load. So, the assessment of the effect of this suspended load on the distribution of aqueous Zr, Hf and REE can be considered negligible, with a result quite similar to that induced by partitioning with sediment. Our focus on the “coarse” colloidal fraction with molecular weight cut-offs between 10 KDa and 450 nm should allow to investigate its resistance to salt-induced coagulation, its organic and/or inorganic nature in a river system dominated by weathering of soluble sediments.

2. STUDIED AREA

South-central Sicily, i.e. the Caltanissetta basin (see Fig. 1), is a NE-SW elongated area about 140 km large, characterised by widespread evaporite outcrops belonging to the Gessoso-solfifera formation. These sediments were deposited as a consequence of the progressive lack of communication between the current Mediterranean Sea and the ocean during the Messinian Salinity Crisis (Hsu et al. 1973). The Caltanissetta basin is included between the northernmost Appenino-Maghrebide range and the easternmost Iblean plateau. The evaporite succession is preceded by diatomites (locally called Tripoli). Diatomites are followed by the lowermost evaporitic unit consists of limestones (locally called "Calcare di Base") followed by laminated gypsum (balatino) and selenite, often embedded with gypsum marls and locally topped by salt deposits. Immediately above the Calcare di Base, a sulphur-bearing limestone locally called "Calcare Solfifero" occurs, consisting of microcrystalline calcite, celestine, aragonite and native sulphur (Dessau et al. 1962). Here, starting from the Roman period, sulphur extraction procedures were carried out, initially by hand. The uppermost evaporite unit consists of laminar, massive and clastic gypsum with marly to clay intercalations followed by a transgressive conglomerate locally called "Arenazzolo" (Manzi et al. 2009). The Messinian Salinity Crisis was ended by the deposition of the Trubi formation consisting of foraminiferal marls corresponding to the reopening of water communication between the evaporitic basin and the open ocean (Rouchy et al. 2001).

The mining exploitation in the Bosco-San Cataldo area began with a sulphur mine between 1930 and 1938. During the exploitation of the sulphur deposit, large landfills were produced close to the mining area. These consisted of wastes formed by detritus of "Calcare solfifero" hosting the sulphur deposit that was roasted to extract sulphur. These materials consist of carbonates (mainly calcite, aragonite and sometimes strontianite) and variable amounts of celestine and gypsum. In 1954, the discovery in the same area of a large kainite deposit led to the conversion of the progressively declining sulphur mine to a more promising salt mine. The kainite exploitation and related industrial

activities involved the accumulation of a large salt landfill up to 1988, when mining activity was interrupted. Now, the studied area shows a characteristic white deposit of salt wastes whose occurrence strongly influences the composition of the surface waters belonging to the Platani river catchment.

The Platani River has the second widest drainage basin in south-central Sicily (1,785 km^2) and flows through the western part of the Caltanissetta basin (Fig. 1) where wide evaporitic sequences crop out. In particular, the Stincone-Salito flow rate is close to about 1 m^3 sec^{-1}.

3. MATERIALS AND METHODS

Samples of 38 river waters were collected along the Platani catchment, starting from the Bosco-San Cataldo mining area. The weathering of these landfills by rainwater has promoted salinization of the higher course of the Platani River, creating the conditions for investigating trace element fractionation between the dissolved pool (consisting of colloids and the truly dissolved fraction) and river sediments in a wide range of ionic strength conditions (Censi et al., 2016). Many water samples were collected along the tributaries of the Platani River; these are creeks rather than rivers and are characterised by limited water depth and turbulent water flows. Therefore, the large suspended particles (larger than 450 nm) were mainly considered as a result of the resuspension of the riverbed sediments and their composition was not investigated in this study. The studied area along the River Platani, its location in South-Central Sicily and the Bosco-S. Cataldo abandoned mining site are reported in Fig. 1.

The field work was carried out during several seasons from 2014 to 2016: December 2014, January 2015, May 2015, April 2016 and October 2016. The Eh, pH, temperature and conductivity of the studied waters were measured directly in the field with an ORION 250+ meter. Eh measurements were carried out with an Eh oxytrode Pt probe (Hamilton™) using a reference standard solution buffer at 0.475±0.005 V. The accuracy of determinations was ±0.01 V for Eh, ±0.1 for pH, ±0.1°C

149 for temperature, and 1% for EC. The major anions were analysed using a Dionex ICS 1100
150 chromatograph on filtered and acidified (HNO_3) samples with a Dionex CS-12A column for cations
151 and on filtered and acidified (HNO_3) samples with a Dionex AS14A column for anions. Alkalinity
152 was determined in the field by titration with HCl 0.1 M. At each sampling site, three litres of water
153 were collected:
154 Two litres were immediately filtered on-field through 450 nm sterile filter membrane
155 (CHM™ cellulose acetate filter) and represented the dissolved fraction (DF). Then, DF was stored in
156 a previous acid-cleaned polyethylene bottle for subsequently separating the colloidal (CF) from the
157 truly dissolved (TDF) fraction by ultrafiltration. The ultrafiltration procedure was carried out was
158 carried out in the lab with a VIVAFLOW 50R® (Sartorius Stedim Biotech GmbH) cross-flow
159 filtration cassette manifold (molecular weight cut-off 10 KDa) with a 50 cm^2 filter surface area and
160 filters made by regenerated cellulose. In detail, the choice of collecting the 10 KDa colloid fraction
161 was made since this coarser fraction usually concentrates Zr, REE and other trace elements relative to
162 the "light" 1 KDa fraction where transition metals are usually associated (Lyven et al., 2003). During
163 the cross-flow filtration, concentration factors (C_f) > 10 were found to be suitable for the
164 determination of the colloidal fraction. C_f values were assessed according to the equation:

165 $$cf = \frac{(Volume_{TDF} + (Volume_{CF}}{(Volume_{CF})} \quad (1)$$

166 (Larsson et al., 2002; Guo and Santschi, 2007). After their collection, TDF was added with 1% ultra-
167 pure HNO_3 solution to attain pH ≈ 2 and then stored for trace element analysis.
168 Another litre of water was collected, acidified with 1% ultra-pure HNO_3 solution to attain pH ≈ 2,
169 and then stored in a polyethylene bottle. This is hereafter defined as the dissolved fraction (DF).
170 Without further treatment, Fe and Mn concentrations were analysed in this fraction.
171 As follows, Zr, Hf and REE in DF and TDF solutions were enriched according to the method
172 reported by Raso et al. (2013). Then, an NH_4OH (25%) solution was added to attain pH 8 in the

aqueous phase and an excess of $FeCl_3$ (1%) solution was added there to induce the precipitation of solid $Fe(OH)_3$. REE, Zr and Hf were scavenged onto the surface of the crystallising $Fe(OH)_3$ and could be separated from the remaining liquid. In order to be sure that the crystallisation of Fe-hydroxide was complete, the solution was left in a closed flask for 48 h and then Fe hydroxide was collected onto a membrane filter (Millipore™ manifold filter diameter 47 mm, pore size 450 nm). Fe hydroxide was dissolved in 3 M HCl. The obtained solution was diluted 1:3 and analysed by quadrupole-ICP-MS (Agilent 7500cc) with an external calibration procedure. The overall concentration factor of investigated elements was approximately 33-fold. The assessment of the analytical precision in the determination of REE, Zr and Hf concentrations was hard to carry out since, to the author's knowledge, aqueous standard reference materials with referenced concentrations of these elements are not available. Hence, following the procedure of Raso et al. (2013), three aliquots (one litre each) of NASS-6 (distributed by the National Research Council of Canada) were treated as water samples according to the above-mentioned procedure and the obtained concentrations were compared with those previously reported in the literature (Jochum et al., 2006; 2008). The results of this procedure are reported in Table S1 of the supplementary on-line material.

REE concentrations were normalised to PAAS (Post Archean Australian Shale) as defined by Taylor and McLennan (1995). Features of shale-normalised patterns were depicted in terms of ratio between heavy REE (HREE) and light REE (LREE) according to the equation:

$$\left|\frac{HREE}{LREE}\right| = \frac{([Ho]+[Er]+[Tm]+[Yb]+[Lu])/5}{([La]+[Ce]+[Pr]+[Nd])/4} \quad (2).$$

The extent of enrichment in intermediate REE (MREE) were calculated in terms of geochemical anomaly according to the equation:

$$\left|\frac{MREE}{MREE*}\right| = \frac{\frac{2x([Sm]+[Eu]+[Gd]+[Tb]+[Dy])}{5}}{\frac{[La]+[Ce]+[Pr]+[Nd]}{4}+\frac{[Ho]+[Er]+[Tm]+[Yb]+[Lu]}{5}} \quad (3).$$

In order to assess possible interferences of BaO^+ on Eu^+ mass, the entire calibration procedure was performed with calibration solutions having a Ba/Eu weight ratio of 10000. Furthermore, during the entire analytical session, in order to evaluate the accuracy of analysis, certified reference waters (Spectrapure Standards, Norway) containing both elements at 2 different concentrations: 0.5 ppb of Eu and 50 ppb of Ba in SPSSW1, 2.5 ppb of Eu and 250 ppb of Ba in SPSSW2 were repeatedly analysed and the results were always within ±10% for both elements.

Following the procedures of Schlosser and Croot (2008) and Kulaksiz and Bau (2013), Zr, Hf and REE concentrations in CF were assessed as difference between their dissolved and truly dissolved concentrations.

All chemicals used during laboratory manipulations were of ultra-pure grade. Ultra-pure water (resistivity of 18.2 Ω cm) was obtained from an EASY pure II purification system (Thermo, Italy). Nitric acid 65% (w/w), ammonia and hydrochloric acid were purchased from VWR International. Working standard solutions for the studied elements were prepared on a daily basis by stepwise dilution of the single-element stock standard solutions provided from CPI International (1000 ± 5 µg ml^{-1}) in 1 M HCl medium.

All labware was made of polyethylene, polypropylene or Teflon and the calibration of all volumetric equipment was performed. A calibrated E42-B balance (Gibertini, Italy) was used to weight all samples and standards. pH measurements were carried out with a HI 991300 pH meter (Hanna Instruments, Italy).

CF samples for SEM observations were obtained according to two different methods. During the first method, 10 ml of collected colloid suspension from selected samples were collected in a 20 ml Falcon vial and ultracentrifuged (20000 rpm for 5 min). Then, the aqueous supernatant was removed and 500 µl of the remaining fully enriched colloidal suspension was transferred onto an aluminium stub previously coated with a graphite disk sticker. Then, the stub was heated at 50°C for 20 minutes to evaporate any water residue. In the second approach, CF samples were ultracentrifuged at 10,000

rpm for 10 min. Then, 500 µl of the colloid fraction were transferred on the graphite-coated aluminium stub and dried at 60°C for 30 min. Both of these methods produced the same effects. The aluminium stub was gold coated and SEM observation and EDS analyses were carried out using a LEO 1430 SEM (Carl Zeiss, Cambridge, UK) equipped with an EDS OXFORD INCA energy-dispersive spectrometric microanalysis system. Quantitative analyses were carried out with 15 kV accelerating voltage, 600 pA beam current and 1 µm beam diameter. Correction of matrix effects was routinely applied. EDS calibration for quantitative analyses was carried out using natural mineral and glass standards.

In order to analyse traces of REE, Zr and Hf in bottom sediments, seven samples were selected. Sample analyses were carried out with sequential extractions using the method proposed by Koschinsky and Halbach (1995). The sequential leaching procedure was used to analyse the concentrations in four different sediment fractions. The procedures are as follows:

- Labile fraction: an aliquot of 1 g of powdered sample was added to 30 ml of an acetic acid solution (1 M), buffered with Na acetate, at room temperature for 5 hours. The solution was filtered through a 450 nm membrane filter, the residual sediment was washed and the filtered solution was brought up to a final volume of 50 ml.
- Easily reducible fraction: 175 ml of a prepared solution of 0.1 M hydroxylamine hydrochloride (pH 2) was added to the residue of step 1 and stirred for 24 hours at 25°C. The final solution was treated as step 1 and the final volume of the filtrate was 200 ml.
- Moderately reducible fraction: the solid residue of step 2 was treated with 175 ml 0.2 M oxalic acid, buffered with ammonia oxalate (3.5 pH) and the mixture was stirred at 25°C for 12 hours.
- Residual-silicate fraction: The final residue of the previous steps was totally digested in Teflon bombs at 180°C for 12 hours, with a solution of 3 ml of 48% HF, 3 ml of 37% HCl

and 1 ml of 65% HNO_3. After digestion, the solution was filtered and Millipore water was added up to a final volume of 50 ml.

According to Koschinsky and Halbach (1995), the leaching solution from the first sediment fraction represents the release of labile bound trace elements and those coming from carbonate minerals. The solution from the second sediment fraction represents the release of trace elements from Mn-bearing phases, probably Mn-oxyhydroxides. The large geochemical coherence between V and Fe suggests that the solution from the third sediment fraction can represent the release of trace elements from Fe-bearing phases. The significant occurrence of Be, Ti, Cr, Co, Ni, Cu, Zr and others in the solution from the fourth fraction is consistent with its origin from the detritic contribution.

An analytical check of data quality was carried out by measuring the Zr, Hf and REE concentrations in five aliquots of MAG-1 (marine sediment reference standard distributed by the United States Geological Survey), only for the total digestion procedure, since the certification of trace element concentrations for MAG-1 is not given for sequential extractions, to our knowledge. The analysis of MAG-1 is reported in Table S1 of the supplementary on-line material and compared with reference data.

The obtained solutions from each procedure were suitably diluted and analysed by quadrupole-ICP-MS (Agilent 7500cc) with an external calibration procedure. All reagents used in the procedures were at least of analytical grade purity.

4. RESULTS

The chemical-physical parameters, major and selected minor element concentrations of the studied waters are reported in Table S3 of supplementary on-line material. The ionic strength (μ) and the Eh values cover a wide range from 0.11 to 5.15 mol kg^{-1} and -0.04 to 0.20 V, respectively. Sample waters are characterized by a wide spectrum of major elements composition related to the nature of evaporitic rocks outcropping in the catchment area (See Table S2 of supplementary on-line material).

4.1 Dissolved fraction <450 nm (DF)

The concentrations of Zr, Hf, Y and Ho measured in DF are provided in Table S4 of the supplementary on-line material. Zirconium and Hf concentrations ranged between 52 and 2529 pmol kg^{-1} and between 0 and 49 pmol kg^{-1}, respectively. Zr/Hf weight ratios were between 50 and 350, although many Zr/Hf values close to the chondritic signature (70.4 ±5.7, Jochum et al., 1986) were measured in samples collected in the middle and lower river paths of the Platani River. Figure 2 shows that Zr and Hf concentrations describe two different linear trends in DF samples. Zr and Hf concentrations measured in waters collected close to the Bosco-San Cataldo mine (samples from PL1 to PL7) fell along a trend line with a slope of 208, whereas other samples fell along a trend line with a slope close to 51. Figure 3A shows that Zr/Hf values in DF samples progressively increased with the ionic strength, starting from slight subchondritic to chondritic values found in samples with $\mu \leq 1$ mol kg^{-1}. Similar results were also observed for the Y/Ho ratio. Figure 3B shows that subchondritic and chondritic Y/Ho values are found in DF samples with a low ionic strength, whereas Y/Ho progressively increased with the ionic strength up to superchondritic terms.

The REE concentration in waters range from 0.3 and 49.1 nmol kg^{-1} with higher REE values occurring along the middle river path. The values of Y/Ho weight ratio are distributed between 25.3 to 90.0. In other places along the river, Y/Ho values were close to the chondritic range of values (52 ± 5; Jochum et al., 1986). Figure 3C shows that the overall REE concentration in DF described an exponential array with the largest REE concentrations being observed in the lowest ionic strength river waters.

The shale-normalised REE patterns of DF samples showed two different features. The first, hereafter defined as a Type I pattern, was characterised by an ascending feature determined by a progressive increase in normalised concentrations along the REE series, whereas the second, defined as a Type II pattern, showed a characteristic MREE enrichment relative to LREE and HREE. Only in two samples

294 were La enrichments shown and some evidence of Ce anomalies observed. Positive Gd anomalies
295 were shown in some river waters from the middle river path (Fig. 4).
296
297 4.2 Colloidal fraction (10 KDa < CF <450 nm)
298 The concentrations of Zr, Hf and REE measured in CF are reported in Table S5 of the supplementary
299 on-line material. Zirconium and Hf concentrations were in the range of 54.2-855.9 pmol kg^{-1} and 0.1-
300 2.5 pmol kg^{-1}, respectively. As a consequence, Zr/Hf values fell within a range of values from 82.3
301 and 525.4. At the same time, Y and Ho concentrations ranged between 23.1 and 230.5 pmol kg^{-1} and
302 from 0.6 and 3.9 pmol kg^{-1}, respectively. The related values of the Y/Ho ratio fall between 24.6 and
303 63.1. The REE concentration in CF was between 109.8 and 810.7 pmol kg^{-1}. Figure 3D shows that
304 the Zr/Hf values in CF progressively increase with increasing ionic strength with the highest value
305 found at about 3.2 mol kg^{-1}. Figure 3E shows that the Y/Ho ratio in CF progressively decreased, with
306 increasing ionic strength from slightly superchondritic to chondritic values towards subchondritic
307 ratios. Figure 3F shows a possible decrease of the overall REE concentration in CF with increasing
308 ionic strength.
309 Figure 5A showed the features of shale-normalised REE patterns. These are characterised by Ce/Ce*
310 values ranging from 0.6 to 2.5, Gd/Gd* values between 1.0 and 3.4 and a slight MREE enrichment in
311 some samples with MREE/MREE* ranging from 0.6 and 1.8 (Table 1). As a consequence, some
312 similarity can be found between the normalised trends in CF shale-normalised Type II patterns.
313 Comparing the feature of shale-normalised patterns from Fig. 5A with those calculated for the
314 corresponding DF samples (Fig. 5C), the observed Gd/Gd* > 1 values in CF may be responsible of
315 the same features observed in DF.
316 The SEM images were carried out on CF samples (Fig. 6A-C) and on suspended solids after filtration
317 at 450 nm (Fig. 6B-D). Figure 6A shows aggregates of grouped nanospheres with a diameter ranging
318 from about 200 to about 400 nm onto the substratum. Microspheres with similar Ca-Mg carbonatic

composition (Fig. 6E) also occurs in suspended fraction (Fig. 6B). EDS analyses carried out on nanoaggregates of crystals collected from CF samples (Fig. 6C) suggest their clayey nature (Fig. 6F). On the contrary, the composition of substratum of colloids shows an Al-Mg-K rich composition (Fig. 6G). These features are observed in almost all the studied samples irrespective of the ionic strength. Fig. 7 shows the texture of colloids concentrated from the PL-26 water sample. According to the X-ray maps of Al and Mg, these materials mainly consisted of Al- and Mg-bearing products. On the contrary, Si was mainly clustered on the left side of the aggregates, together with Ca-bearing materials. Fe was scattered everywhere, suggesting the coating nature of Fe-bearing products.

4.3 Truly dissolved fraction (TDF < 10 KDa)

The concentrations of Zr, Hf and REE measured in TDF from the studied water samples are reported in Table S5 of the supplementary on-line material. The Zr concentration was between 37.3 and 259.8 pmol kg^{-1}, whereas the Hf content ranged between 0.6 and 1.7 pmol kg^{-1}. The related Zr/Hf values fell between 66.5 and 275.9, with higher values measured in high ionic strength samples. The Y and Ho concentrations in TDF (6.7 and 303.7 pmol kg^{-1}, 0.6 and 3.0 pmol kg^{-1}, respectively) were lower than those found in CF. The Y/Ho weighted ratio values ranged from 44.8 and 101.2, similar to those found in DF and CF. Figure 3D, E and F show that the Zr/Hf, Y/Ho and REE concentrations in TDF progressively increased with the ionic strength.

The shale-normalised REE patterns in TDF of some samples were different relative to those observed in CF (Fig. 5B) since they often showed negative Ce anomaly values (Table 1) and more pronounced ascending behaviour along the REE series, than those observed in the Type I pattern of DF samples. Only two samples show the abovementioned MREE enrichment. and neither Ce nor Gd anomalies were reported. The latter finding confirms that the observed $Gd/Gd^* > 1$ values in DF (Fig. 5C) are determined by the colloidal fraction occurring in the dissolved pool.

Figure 5D summarises the features of shale-normalised REE patterns in DF, CF e TDF. TDF are characterised by MREE depleted patterns (MREE/MREE* ≤ 1) and large HREE/LREE fractionation. CF shows moderately MREE enriched patterns associated to the lesser extent of HREE/LREE fractionation than TDF. On the contrary, DF samples are distributed along a curved array and show the largest observed MREE/MREE* features.

4.4 Sediment

The mineralogical composition of the sediments showed gypsum, calcite, dolomite, celestine, boehmite and rare strontianite in the coarse (> 2 µm) fraction, whereas montmorillonite and kaolinite occurred in the fine (< 2 µm) fraction (Fig. 8). A similar composition was observed in suspended particulates (> 450 nm) where the X-ray maps obtained by EDS analyses showed that the finest particles were formed of Si-Al bearing clays, whereas Ca, Mg-carbonates and gypsum occurred among the coarser subangular fragments of suspended solids (Fig. 9).

The concentrations of Zr, Hf and REE measured in different extracted sediment fractions from the collected samples are reported in Table S6 of the supplementary on-line material. Zirconium concentrations ranged between 0.1 and 0.2 µmol kg^{-1} whereas Hf around 0.01 µmol kg^{-1} in the first sediment fraction. Here, REE concentrations ranged from 27.5 and 41.8 µmol kg^{-1}. Zirconium concentrations ranged from 0.01 and 0.1 µmol kg^{-1} whereas Hf was between 0.00 and 0.001 µmol kg^{-1} in the second sediment fraction. In these solids, REE concentrations ranged from 1.8 and 4.1 µmol kg^{-1}. In the third sediment fraction, Zr concentrations were between 1.1 and 7.0 µmol kg^{-1} whereas Hf was between 0.01 and 0.12 µmol kg^{-1}. The REE content of these materials was 3.6 to 22.9 µmol kg^{-1}. In the detritic component represented by the fourth sediment fraction, the largest trace element concentrations are shown: the Zr content was between 164.5 and 1532 µmol kg^{-1} whereas Hf ranged from 2.3 to 20.1 µmol kg^{-1}. The REE concentrations ranged between 19.8 and 533.8 µmol kg^{-1}. Related Zr/Hf values fell within the following ranges for the first fraction (43.5-117.7), second

fraction (92.7-170.9), third fraction (51.1-86.1) and fourth fraction (71.6-79.9). Figure 10 shows that the Zr and Hf concentrations in the studied fractions fell along the same a linear trend characterised by a chondritic slope.

Y/Ho values were clustered around the chondritic range of values or slight higher in the third and fourth sediment fractions, whereas slight superchondritic values were found in the first and second fractions. The shale-normalised REE patterns of sediment fractions showed MREE enrichments in the first and third fractions and were almost flat in shape in the second and fourth fractions (Fig. 11). In the second fraction, almost all the studied samples showed a positive Eu anomaly that was also recognised in the fourth sediment fraction. The flat behaviour of the REE patterns in the fourth fraction was also observed in evaporite outcroppings in the surroundings. Although the features of the shale-normalised patterns in the sediment fractions were similar, the HREE/LREE fractionation in the first (and partially in the fourth) fraction was lower than those observed in second and third fractions (Fig. 11). All the samples were free from positive Ce anomalies. In the second fraction, the shape of the shale-normalised patterns was flatter, with a lesser extent of MREE enrichment. Instead, there were strong positive Eu anomalies ranging from 1.40 and 3.73. In the third sediment fraction, Ce/Ce* values were close to 1 and no significant Ce anomalies were observed. In the fourth fraction, positive Ce anomalies were shown ($1.11 \leq Ce/Ce^* \leq 2.12$), sometimes with positive Eu anomalies attaining 5.32.

5. Discussion

5.1 Nature of colloids in studied waters

The lack of organic SEM observations carried out on the separated colloidal fraction suggests the mainly inorganic nature of the 10 KDa colloidal fraction that consists of nanoparticles aggregated of Al-oxyhydroxides, clay minerals and carbonate (Fig. 6). The occurrence of colloidal nanoaggregates also under high ionic strength conditions can be explained with pseudohydrophilic behaviour of Al-

oxyhydroxides (Volkova et al., 2017). In these waters, the apparent lack of organic colloids is probably determined either by their coagulation under high ionic strength conditions, or by the fractionation of a humic-like fine colloidal fraction in TDF rather than in the 10 KDa coarse fraction (Liu et al., 2016).

5.2 Zr, Hf and REE distribution between colloids and truly dissolved fraction

Zr/Hf values larger than the chondritic signature calculated for studied colloids suggest a larger affinity of aqueous Zr rather than Hf species towards colloid surfaces. This hypothesis is rather strange considering that usually the higher Hf affinity than Zr towards available surfaces was observed during interface processes driven by coulombic interactions (Koschinsky and Hein, 2003; Godfrey et al., 2008; Bau and Alexander, 2009; Schmidt et al., 2014; Censi et al., 2017). In natural waters, the dissolved Zr and Hf speciation is usually determined by hydroxyl-complexes, at least if an ionic strength less than 2 mol kg^{-1} occurs (Aja et al., 1995; Veyland et al., 1998; Byrne, 2002; Ekberg et al., 2004; Qiu et al., 2009; Wang and Lee, 2016). Under these conditions, $(Zr(H_2O)_4(OH)_4)$ and $(Hf(H_2O)_3(OH)_5)^-$ complexes seem to be the most stable Zr and Hf species under alkaline conditions (Jahn et al., 2015) and the preferential Hf scavenging relative to Zr would occur onto positively charged surfaces. Colloid nanoaggregates recognised in studied waters consist of Al-oxyhydroxides having a zero-point charge between 5.7 to about 10 in pH scale, depending from the mineralogy Al-bearing solid formed by diaspore or boehmite and gibbsite, respectively (Stumm, 1992; Kosmulski, 2002; 2016; Mui et al., 2016). Therefore, if diaspore is the most abundant phase in Al-oxyhydroxide nanoaggregates, its surface would have a negative charge at the measured pH values and the preferential Hf scavenging relative to Zr would not occur. So, if the recognised relationship between pH values and Zr/Hf ratio in CF materials (Fig. 12) represents a confirmation that the interactions between the Zr-Hf complexes and nanoaggregate surface have a coulombic nature (Smith, 1999), it

417 also suggests that the extent of Zr-Hf decoupling may be also influenced by the mineralogy of Al-
418 oxyhydroxides.
419 The shale-normalised REE patterns of the studied colloids are characterised by LREE depletion
420 similar to those recognised in previous studies (Sholkovitz, 1992; 1995; Bertine and VernonClark,
421 1996; Pokrovsky et al., 2005). Probably, in studied colloids the LREE depletion is consistent with
422 the presence of detritic dolomite eroded from marine evaporites that usually shows LREE-depleted
423 shale-normalised patterns (Meyer et al., 2012). Otherwise, since the shale-normalised REE patterns
424 in TDF are affected by LREE depletion, this phenomenon could be a consequence of preferential
425 LREE sequestration onto Fe-oxyhydroxides, as modelled by Schijf et al. (2015). This is probably
426 disseminated onto surfaces of nanoaggregates as indicated by the Fe distribution shown by the X-ray
427 map (Fig. 7) and by the observed X-ray lines of Fe in the EDS spectra (Fig. 6).
428 The concurrent effect of changes in REE concentration and Zr/Hf ratio in DF of studied waters is
429 reported in Fig. 13A where allows to depict a hyperbolic array. This evidence suggests that the
430 changes of REE concentration and Zr/Hf values are determined by the combination of two opposite
431 circumstances. The first one (EM-1) characterised by high REE concentrations and chondritic to
432 subchondritic Zr/Hf values. The second one (EM-2) where high Zr/Hf values are coupled to low REE
433 concentrations. The companion plot constructed reporting Zr/Hf values vs. 1/[REE] shows a linear
434 array (Fig. 13B) confirming that shown in Fig. 13A effectively represents a mixing hyperbola
435 (Langmuir et al., 1978; Albarede, 1996 for a comprehensive review). Only high ionic strength waters
436 collected close to the Bosco-San Cataldo mine fell outside the trend in the companion plot (Fig.
437 13B).
438 Similar features observed in Fig. 13A are also shown in Fig. 14. Here, the largest Al, Fe and REE
439 concentrations in DF are found in samples with ionic strength less than 0.5 mol kg^{-1}, whereas lower
440 concentrations of the aforementioned metal ions are found in waters with $\mu > 1$ mol kg^{-1}. Taking into
441 account that the largest colloid content in DF should occur under low ionic strength conditions

(Sholkovitz, 1993; 1995; Merschel et al., 2017 and references therein) and metal ions should mainly occur as aqueous specie in TDF under high ionic strength waters, this distribution easily mirrors the Al, Fe and REE distribution between CF and TDF. Accordingly, the distribution of REE and Zr/Hf values in Fig. 12A could be influenced by the fractionation of these metal ions between CF and TDF.

5.3 The role of sediment fractions on the composition of river waters

The Zr/Hf signature in DF is not driven only by interactions between TDF and CF. The surface of suspended solids and sediment represents suitable interfaces where Zr and Hf can decouple each other. Zr/Hf values in the 1st sediment fraction decrease up to subchondritic values as pH is 8 (Fig. 15A). At the same time, Fig. 15B shows that the same Zr/Hf values are related to the dolomite saturation index. Then, considering that the 1st sediment fraction is considered representative of the leaching of labile phases and carbonates (Koschinsky and Halbach, 1995; Koschinsky and Hein, 2003; Bau and Koschinsky, 2006), the considered change from superchondritic to subchondritic values of Zr/Hf values can be influenced by the change of surface charge from positive to negative of dolomite that occurs at pH = 8 (Pokrovsky et al., 1999).

Type 1 patterns are shown in both the DF of high ionic strength waters (Fig. 4) and in TDF (Fig. 5B), probably since DF and TDF practically coincide in high ionic strength waters, with a very low CF in these waters. The qualitative calculation of REE speciation suggests that $[REE(CO_3)]^+$ was the most stable complex in the studied river waters; this finding agrees with the observed "ascending" feature characteristic of Type I patterns (Cantrell and Byrne, 1987; Lee and Byrne, 1993; Liu and Byrne, 1998). Under higher ionic strength conditions, $[REE(CO_3)]^+$ is associated with $[REECl]^{2+}$ complexes for Ce and Pr and with $[REE(SO_4)]^+$ species for La, Nd and Sm.

If Zr/Hf values measured in the 2nd sediment fraction are compared with pH, only superchondritic values poorly related with pH are observed (Fig. 15 C). This evidence confirms that this fraction is representative of Mn-bearing phases (Koschinsky and Halbach, 1995), poorly reactive towards Zr

and Hf, at least according to coulombic mechanism (Koschinsky and Hein, 2003; Koschinsky and Hein, 2017) and only through impurities of Fe-rich products that preferentially lead to Hf scavenging rather than Zr. The small effect size of the observed relationship between Zr/Hf and pH values in the 2nd sediment fraction could be due to the variability of composition of Mn-bearing solids showing points of zero-point-charge changing in a wide pH range (Kosmulski, 2016).

Although to a lesser extent, shale-normalised REE patterns in the 2nd sediment fraction show features similar to type II patterns with a fractionation along the REE series showing MREE > LREE ≥ HREE (Fig. 11). These features are similar to those shown by Mn-oxyhydroxides in Mn-Fe crusts and hydrogenetic Mn-Fe nodules (Bau et al., 2014; Xiao et al., 2017 for a comprehensive review). Y/Ho values in this fraction are slightly higher than the chondritic values, suggesting a larger Y affinity relative to Ho towards the 2nd sediment fraction. This is the same evidence recognised by Bau and Koschinsky (2009), who explained it by the occurrence of impurities of Fe-oxyhydroxides in these materials that preferentially retain Ho, leaving Y that is adsorbed onto Mn-rich products. Features of shale-normalised patterns from the 2nd sediment fraction reported in Bau and Koschinsky (2009) are very similar to the patterns obtained from leachates of the 2nd sediment fraction. The main difference observed is the large positive Ce anomaly that is not found in our samples. We suggest that the lack of Ce anomaly can be determined by the organic content of pore waters of sediment where oxidized Ce^{IV} is retained onto surfaces of humic matter (Pourret et al., 2008). According to Liu et al. (2016), this hypothesis is consistent with the observed Ce/Ce* >1 values in some TDF samples (Fig. 5) and confirms that the fine humic-like colloidal fraction of studied waters remained associated to TDF during the collection of 10 KDa fraction (Liu et al., 2016).

In the 3rd sediment fraction, pH changes towards more alkaline terms drive the growth of Zr/Hf ratio from subchondritic to chondritic values (Fig. 15D) in the opposite direction from the phenomenon recognised for the 1st sediment fraction (Fig. 15A). This evidence is consistent with the preferential Hf uptake relative to Zr, favoured by the positively charged surface of Fe-oxyhydroxides

(Koschinsky and Hein, 2003; 2017; Bau and Koschinsky, 2006; Hein et al., 2013). This hypothesis agrees with the Zr/Hf value, close to the chondritic signature only at pH = 8.6.

Features of shale-normalised REE patterns in this sediment fraction show an almost symmetrical MREE enriched distribution (Fig. 11). It is characteristic of Fe-rich sediments that preferentially fractionate these elements relative to LREE and HREE (Bau, 1999). The authigenic/diagenetic origin of Fe-solids from the 3rd sediment fraction agrees with the lack of positive Ce anomaly that is usually found in Fe-oxyhydroxides (Bau et al., 2014), and with the alkaline pH conditions of river waters that determine the precipitation of Fe-oxyhydroxides free from positive Ce anomalies (Bau, 1999). According to the above-mentioned preferential fractionation of Ho relative to Y onto Fe-oxyhydroxides (Bau, 1999; Ohta and Kawabe, 2001; Bau and Koschinsky, 2009), Y/Ho values in the 3rd sediment fraction are subchondritic. The abundance of Fe-oxyhydroxides in river sediments is probably the reason for the subchondritic signature of several river sediments (Censi et al., 2007; Viers et al 2008; Garzanti et al., 2010; 2011; Roddaz et al., 2014).

The growth of ionic strength up to 0.7 mol kg^{-1} in studied waters involves the preferential Zr fractionation in CF coupled with the Hf partition in TDF. This phenomenon seems influenced both by pH of waters and mineralogical composition of colloidal nanoaggregates determining whether Zr/Hf values in CF and TDF fall within the range of those measured by Godfrey et al. (2008) in the estuary of the Hudson river. As the highest μ values exceed 0.7 mol kg$^{-1,}$ Zr/Hf values further grow. Considering the larger reactivity of Hf than Zr to Fe-oxyhydroxides and indications provided by Bau and Koschinsky (2006) and Godfrey et al. (2008), the coagulation of colloidal nanoaggregates under ionic strength exceeding that typical of seawater preferentially leads to Hf release rather than Zr, followed by its scavenging onto authigenic Fe-oxyhydroxides in sediments.

6. Concluding remarks

The results of this study indicate that the colloidal fraction dispersed in natural waters withstands dissolved salt levels in excess of 200 g l^{-1}, although the amount decreases with increasing ionic strength, as suggested by Al, Fe, REE concentrations in the DF of the studied waters. This evidence can be explained by the inorganic nature of nanoparticles and colloid nanoaggregates formed by Al-oxyhydroxides, carbonate spherules and clay minerals. The humic-like colloidal fraction was not found in CF and seems partitioned in TDF due to its fine size.

As ionic strength exceeds 0.7 mol kg^{-1}, Al-oxyhydroxides-based nanoaggregates become progressively less stable, probably as a result of incipient colloidal coagulation. This process results in larger Hf release from CF to TDF than Zr that is followed by preferential Hf scavenging onto authigenic Fe-oxyhydroxides in bottom sediments. Therefore, the occurrence of a coarse inorganic Al-oxyhydroxide colloidal fraction associated with the Fe-oxyhydroxide fraction of river sediment seems to induce a Zr-Hf decoupling during the growth of ionic strength. This could represent the early stage of larger Zr-Hf fractionations occurring along the seawater column. Therefore, Zr/Hf ratios far from the chondritic range of values can be expected in authigenic minerals. The main character that seems to highlight the influence of the Al-rich inorganic colloids relative to the organic colloidal component is their stability under ionic strength conditions overcoming those characterising seawater. Further studies are needed for corroborating this scenario. They should be focused on the recognition of Zr and Hf behaviour in dissolved pools of coastal seawater

Acknowledgments

This work was financially supported by the grants CORI 2012 of University of Palermo and n° 2015-COMM-0006 funded by the SIDERCEM S.R.L. - University of Palermo Agreement. We thank the Istituto Nazionale di Geofisica e Vulcanologia—Palermo (INGV) for the analytical support during the analysis of river waters. This paper reports scientific results belonging to the PhD project of Fabio

Sposito. The authors are strongly indebted with the editor and two anonymous reviewers who improved the quality of the original manuscript.

REFERENCES

Aja, S.U., Wood, S.A., Williams-Jones, A.E., 1995. The aqueous geochemistry of Zr and the solubility of some Zr-bearing minerals. Applied Geochemistry 10, 603-620.

Albarède, F., 1995. Introduction to Geochemical Modelling.

Barroux, G., Sonke, J.E., Boaventura, G., Viers, J., Godderis, Y., Bonnet, M.P., Sondag, F., Gardoll, S., Lagane, C., Seyler, P., 2006. Seasonal dissolved rare earth element dynamics of the Amazon River main stem, its tributaries, and the Curuai floodplain. Geochemistry Geophysics Geosystems 7.

Bau, M., 1996. Controls on the fractionation of isovalent trace elements in magmatic and aqueous systems: Evidence from Y/Ho, Zr/Hf, and lanthanide tetrad effect. Contributions to Mineralogy and Petrology 123, 323-333.

Bau, M., 1999. Scavenging of dissolved yttrium and rare earths by precipitating iron oxyhydroxide: Experimental evidence for Ce oxidation, Y-Ho fractionation, and lanthanide tetrad effect. Geochimica et Cosmochimica Acta 63, 67-77.

Bau, M., Alexander, B.W., 2009. Distribution of high field strength elements (Y, Zr, REE, Hf, Ta, Th, U) in adjacent magnetite and chert bands and in reference standards FeR-3 and FeR-4 from the Temagami iron-formation, Canada, and the redox level of the Neoarchean ocean. Precambrian Research 174, 337-346.

Bau, M., Koschinsky, A., 2006. Hafnium and neodymium isotopes in seawater and in ferromanganese crusts: The "element perspective". Earth and Planetary Science Letters 241, 952-961.

Bau, M., Koschinsky, A., 2009. Oxidative scavenging of cerium on hydrous Fe oxide: Evidence from the distribution of rare earth elements and yttrium between Fe oxides and Mn oxides in hydrogenetic ferromanganese crusts. Geochemical Journal 43, 37-47.

565 Bau, M., Schmidt, K., Koschinsky, A., Hein, J., Kuhn, T., Usui, A., 2014. Discriminating between
566 different genetic types of marine ferro-manganese crusts and nodules based on rare earth elements
567 and yttrium. Chemical Geology 381, 1-9.
568 Bertine, K.K., VernonClark, R., 1996. Elemental composition of the colloidal phase isolated by
569 cross-flow filtration from coastal seawater samples. Marine Chemistry 55, 189-204.
570 Byrne, R.H., 2002. Inorganic speciation of dissolved elements in seawater: The influence of pH on
571 concentration ratios. Geochemical Transactions 3, 11-16.
572 Cantrell, K.J., Byrne, R.H., 1987. Temperature dependence of europium carbonate complexation.
573 Journal of Solution Chemistry 16, 555-566.
574 Censi, P., Cangemi, M., Brusca, L., Madonia, P., Saiano, F., Zuddas, P., 2015. The behavior of rare-
575 earth elements, Zr and Hf during biologically-mediated deposition of silica-stromatolites and
576 carbonate-rich microbial mats. Gondwana Research 27.
577 Censi, P., Inguaggiato, C., Chiavetta, S., Schembri, C., Sposito, F., Censi, V., Zuddas, P., 2017. The
578 behaviour of zirconium, hafnium and rare earth elements during the crystallisation of halite and other
579 salt minerals. Chemical Geology 453, 80-91.
580 Censi, P., Sposito, F., Inguaggiato, C., Venturi, M., Censi, V., Falcone, E.E., 2016. Weathering of
581 evaporites: natural versus anthropogenic signature on the composition of river waters. Rendiconti
582 Lincei 27, 29-37.
583 Censi, P., Sprovieri, M., Saiano, F., Di Geronimo, S.I., Larocca, D., Placenti, F., 2007. The behaviour
584 of REEs in Thailand's Mae Klong estuary: Suggestions from the Y/Ho ratios and lanthanide tetrad
585 effects. Estuarine, Coastal and Shelf Science 71, 569-579.
586 Censi, P., Zuddas, P., Randazzo, L.A., Saiano, F., Mazzola, S., Aricò, P., Cuttitta, A., Punturo, R.,
587 2010. Influence of dissolved organic matter on rare earth elements and yttrium distributions in coastal
588 waters. Chemistry and Ecology 26, 123-135.

589 Cidu, R., Frau, F. 2009. Influence of the fine-particle load in Mediterranean rivers and streams on the
590 distribution of trace elements in filtered and not filtered aqueous fractions. Applied Geochemistry,
591 24, 611-623
592 Dessau, G., Jensen, M.L., Nakai, N., 1962. Geology and isotopic studies of Sicilian sulfur deposits.
593 Economic Geology 57(3), 410-438.
594 Ekberg, C., Källvenius, G., Albinsson, Y., Brown, P.L., 2004. Studies on the hydrolytic behavior of
595 zirconium(IV). Journal of Solution Chemistry 33, 47-79.
596 Elbaz-Poulichet, F., Dupuy, C., 1999. Behaviour of rare earth elements at the freshwater-seawater
597 interface of two acid mine rivers: the Tinto and Odiel (Andalucia, Spain). Applied Geochemistry 14,
598 1063-1072.
599 Elderfield, H., 1988. On understanding sediment geochemistry. Applied Geochemistry 3, 110.
600 Elderfield, H., Greaves, M.J., 1982. The rare earth elements in seawater. Nature 296, 214-219.
601 Elderfield, H., Upstill-Goddard, R., Sholkovitz, E.R., 1990. The rare earth elements in rivers,
602 estuaries, and coastal seas and their significance to the composition of ocean waters. Geochimica et
603 Cosmochimica Acta 54, 971-991.
604 Firdaus, M.L., Minami, T., Norisuye, K., Sohrin, Y., 2011. Strong elemental fractionation of Zr-Hf
605 and Nb-Ta across the Pacific Ocean. Nature Geoscience 4, 227-230.
606 Frank, M., 2011. Oceanography Chemical Twins, Separated. Nature Geoscience 4, 220-221.
607 Garzanti, E., Andó, S., France-Lanord, C., Vezzoli, G., Censi, P., Galy, V., Najman, Y., 2010.
608 Mineralogical and chemical variability of fluvial sediments. 1. Bedload sand (Ganga-Brahmaputra,
609 Bangladesh). Earth and Planetary Science Letters 299, 368-381.
610 Garzanti, E., Andó, S., France-Lanord, C., Censi, P., Vignola, P., Galy, V., Lupker, M., 2011.
611 Mineralogical and chemical variability of fluvial sediments 2. Suspended-load silt (Ganga-
612 Brahmaputra, Bangladesh). Earth and Planetary Science Letters 302, 107-120.

613 Godfrey, L.V., Field, M.P., Sherrell, R.M., 2008. Estuarine distributions of Zr, Hf, and Ag in the
614 Hudson River and the implications for their continental and anthropogenic sources to seawater.
615 Geochemistry, Geophysics, Geosystems 9.
616 Godfrey, L.V., White, W.M., Salters, V.J.M., 1996. Dissolved zirconium and hafnium distributions
617 across a shelf break in the northeastern Atlantic Ocean. Geochimica et Cosmochimica Acta 60, 3995-
618 4006.
619 Goldstein, S.J., Jacobsen, S.B., 1988. Rare earth elements in river waters. Earth and Planetary
620 Science Letters 89, 35-47.
621 Guo L., Santschi P.H., 2007. Ultrafiltration and its Applications to Sampling and Characterisation of
622 Aquatic Colloids. In: Wilkinson K . J . and Lead J . R. eds.: Environmental Colloids and Particles:
623 Behaviour, Separation and Characterisation. IUPAC Series on Analytical and Physical Chemistry
624 Vol. 10, pp 160-221.
625 Hannigan, R.E., Sholkovitz, E.R., 2001. The development of middle rare earth element enrichments
626 in freshwaters: Weathering of phosphate minerals. Chemical Geology 175, 495-508.
627 Hein, J.R., Mizell, K., Koschinsky, A., Conrad, T.A., 2013. Deep-ocean mineral deposits as a source
628 of critical metals for high- and green-technology applications: Comparison with land-based
629 resources. Ore Geology Reviews 51, 1-14.
630 Hsü, K.J., Ryan, W.B.F., Cita, M.B., 1973. Late miocene desiccation of the mediterranean. Nature
631 242(5395), 240-244.
632 Inguaggiato, C., Censi, P., Zuddas, P., D'Alessandro, W., Brusca, L., Pecoraino, G., Bellomo, S.,
633 2016. Zirconium-hafnium and rare earth element signatures discriminating the effect of atmospheric
634 fallout from hydrothermal input in volcanic lake water. Chemical Geology 433, 1-11.
635 Inguaggiato, C., Censi, P., Zuddas, P., Londono, J.M., Chacon, Z., Alzate, D., Brusca, L.,
636 D'Alessandro, W., 2015. Geochemistry of REE, Zr and Hf in a wide range of pH and water

637 composition: The Nevado del Ruiz volcano-hydrothermal system (Colombia). Chemical Geology
638 417, 125-133.
639 Inguaggiato, C., Iñigueza, E., Peiffera, L., Kretzschmar, T., Brusca, L., Mora-Amador, R., Ramirez,
640 C., Bellomo, S., Gonzalez, G., Rouwet, D., 2018. REE fractionation during the gypsum
641 crystallization in hyperacid sulphate-rich brine: The Poás Volcano crater lake (Costa Rica) exploited
642 as laboratory. Gondwana Research, 59, 87-96.
643 Jahn, S., Dubrail, J., Wilke, M., 2015. Complexation of Zr and Hf monomers in supercritical aqueous
644 solutions: Insights from ab initio molecular dynamics simulations. Chemical Geology 418, 30-39.
645 Jochum, K.P., Brueckner, S.M., 2008. Reference Materials in Geoanalytical and Environmental
646 Research - Review for 2006 and 2007. Geostandards and Geoanalytical Research 32, 405-452.
647 Jochum, K.P., Seufert, H.M., Spettel, B., Palme, H., 1986. The solar-system abundances of Nb, Ta,
648 and Y, and the relative abundances of refractory lithophile elements in differentiated planetary
649 bodies. Geochimica et Cosmochimica Acta 50, 1173-1183.
650 Jochum, K.P., Willbold, M., 2006. Reference materials in geoanalytical research - Review for 2004
651 and 2005. Geostandards and Geoanalytical Research 30, 143-156.
652 Johannesson, K.H., Palmore, C.D., Fackrell, J., Prouty, N.G., Swarzenski, P.W., Chevis, D.A.,
653 Telfeyan, K., White, C.D., Burdige, D.J., 2017. Rare earth element behavior during groundwater–
654 seawater mixing along the Kona Coast of Hawaii. Geochimica et Cosmochimica Acta 198, 229-258.
655 Koschinsky, A., Halbach, P., 1995. Sequential leaching of marine ferromanganese precipitates:
656 Genetic implications. Geochimica et Cosmochimica Acta 59, 5113-5132.
657 Koschinsky, A., Hein, J.R., 2003. Uptake of elements from seawater by ferromanganese crusts:
658 Solid-phase associations and seawater speciation. Marine Geology 198, 331-351.
659 Koschinsky, A., Hein, J.R., 2017. Marine ferromanganese encrustations: Archives of changing
660 oceans. Elements 13, 177-182.

661 Kosmulski, M., 2016. Isoelectric points and points of zero charge of metal (hydr)oxides: 50 years
662 after Parks' review. Advances in Colloid and Interface Science 238, 1-61.
663 Kosmulski, M., 2002. The pH-dependent surface charging and the points of zero charge. Journal of
664 Colloid and Interface Science 253, 77-87.
665 Kulaksiz, S., Bau, M., 2007. Contrasting behaviour of anthropogenic gadolinium and natural rare
666 earth elements in estuaries and the gadolinium input into the North Sea. Earth and Planetary Science
667 Letters 260, 361-371.
668 Kulaksiz, S., Bau, M., 2011. Rare earth elements in the Rhine River, Germany: First case of
669 anthropogenic lanthanum as a dissolved microcontaminant in the hydrosphere. Environment
670 International 37, 973-979.
671 Kulaksiz, S., Bau, M., 2013. Anthropogenic dissolved and colloid/nanoparticle-bound samarium,
672 lanthanum and gadolinium in the Rhine River and the impending destruction of the natural rare earth
673 element distribution in rivers. Earth and Planetary Science Letters 362, 43-50.
674 Langmuir, C.H., Vocke Jr, R.D., Hanson, G.N., Hart, S.R., 1978. A general mixing equation with
675 applications to Icelandic basalts. Earth and Planetary Science Letters 37, 380-392.
676 Larsson, J., Gustafsson, Ö., Ingri, J., 2002. Evaluation and optimization of two complementary cross-
677 flow ultrafiltration systems toward isolation of coastal surface water colloids. Environmental Science
678 and Technology 36(10), 2236-2241.
679 Lawrence, M.G., Kamber, B.S., 2006. The behaviour of the rare earth elements during estuarine
680 mixing-revisited. Marine Chemistry 100, 147-161.
681 Lee, J.H., Byrne, R.H., 1993. Complexation of Trivalent Rare-Earth Elements (Ce, Eu, Gd, Tb, Yb)
682 by Carbonate Ions. Geochimica et Cosmochimica Acta 57, 295-302.
683 Liu, R.X., Liu, N.N., Liu, X.L., Yu, H.B., Li, B., Song, Y.H., 2016. Spectroscopic and microscopic
684 characteristics of natural aquatic nanoscale particles from riverine waters. Journal of Geochemical
685 Exploration 170, 10-20.

686 Liu, X.W., Byrne, R.H., 1997. Rare earth and yttrium phosphate solubilities in aqueous solution.
687 Geochimica et Cosmochimica Acta 61, 1625-1633.
688 Lutfi Firdaus, M., Norisuye, K., Nakagawa, Y., Nakatsuka, S., Sohrin, Y., 2008. Dissolved and labile
689 particulate Zr, Hf, Nb, Ta, Mo and W in the western North Pacific Ocean. Journal of Oceanography
690 64, 247-257.
691 Lyvén, B., Hassellöv, M., Turner, D.R., Haraldsson, C., Andersson, K., 2003. Competition between
692 iron- and carbon-based colloidal carriers for trace metals in a freshwater assessed using flow field-
693 flow fractionation coupled to ICPMS. Geochimica et Cosmochimica Acta 67(20), 3791-3802.
694 Manzi, V., Lugli, S., Roveri, M., Charlotte Schreiber, B., 2009. A new facies model for the Upper
695 Gypsum of Sicily (Italy): Chronological and palaeoenvironmental constraints for the Messinian
696 salinity crisis in the Mediterranean. Sedimentology 56, 1937-1960.
697 McKelvey, B.A., Orians, K.J., 1993. Dissolved zirconium in the North Pacific Ocean. Geochimica et
698 Cosmochimica Acta 57, 3801-3805.
699 McKelvey, B.A., Orians, K.J., 1998. The determination of dissolved zirconium and hafnium from
700 seawater using isotope dilution inductively coupled plasma mass spectrometry. Marine Chemistry 60,
701 245-255.
702 Medas, D., Cidu, R., De Giudici, G., Podda, F. 2013. Geochemistry of rare earth elements in water
703 and solid materials at abandoned mines in Sardinia (Italy). J Geochemical Exploration, 133: 149-159.
704 Merschel, G., Bau, M., Dantas, E.L., 2017. Contrasting impact of organic and inorganic nanoparticles
705 and colloids on the behavior of particle-reactive elements in tropical estuaries: An experimental
706 study. Geochimica et Cosmochimica Acta 197, 1-13.
707 Meyer, E.E., Quicksall, A.N., Landis, J.D., Link, P.K., Bostick, B.C., 2012. Trace and rare earth
708 elemental investigation of a Sturtian cap carbonate, Pocatello, Idaho: Evidence for ocean redox
709 conditions before and during carbonate deposition. Precambrian Research 192-95, 89-106.

710 Mui, J., Ngo, J., Kim, B., 2016. Aggregation and colloidal stability of commercially available
711 Al<inf>2</inf>O<inf>3</inf>nanoparticles in aqueous environments. Nanomaterials 6.
712 Nozaki, Y., Lerche, D., Alibo, D.S., Snidvongs, A., 2000. The estuarine geochemistry of rare earth
713 elements and indium in the Chao Phraya River, Thailand. Geochimica et Cosmochimica Acta 64,
714 3983-3994.
715 Ohta, A., Kawabe, I., 2001. REE(III) adsorption onto Mn dioxide (delta-MnO2) and Fe
716 oxyhydroxide: Ce(III) oxidation by delta-MnO2. Geochimica et Cosmochimica Acta 65, 695-703.
717 Osborne, A.H., Hathorne, E.C., Schijf, J., Plancherel, Y., Böning, P., Frank, M., 2017. The potential
718 of sedimentary foraminiferal rare earth element patterns to trace water masses in the past.
719 Geochemistry, Geophysics, Geosystems 18(4), 1550-1568.
720 Pokrovsky, O.S., Dupré, B., Schott, J., 2005. Fe–Al–organic Colloids Control of Trace Elements in
721 Peat Soil Solutions: Results of Ultrafiltration and Dialysis. Aquatic. Geochem. 11, 241-278.
722 Pokrovsky, O.S., Schott, J., Thomas, F., 1999. Dolomite surface speciation and reactivity in aquatic
723 systems. Geochimica et Cosmochimica Acta 63, 3133-3143.
724 Pokrovsky, O.S., Shirokova, L.S., Viers, J., Gordeev, V.V., Shevchenko, V.P., Chupakov, A.V., et
725 al., 2014. Fate of colloids during estuarine mixing in the Arctic. Ocean Science 10(1), 107-125.
726 Pokrovsky, O.S., Viers, J., Shirokova, L.S., Shevchenko, V.P., Filipov, A.S., Dupré, B., 2010.
727 Dissolved, suspended, and colloidal fluxes of organic carbon, major and trace elements in the
728 Severnaya Dvina River and its tributary. Chemical Geology 273, 136-149.
729 Pourret, O., Davranche, M., Gruau, G., Dia, A., 2008. New insights into cerium anomalies in
730 organic-rich alkaline waters. Chemical Geology 251, 120-127.
731 Qiu, L., Guzonas, D.A., Webb, D.G., 2009. Zirconium dioxide solubility in high temperature aqueous
732 solutions. Journal of Solution Chemistry 38, 857-867.

733 Raso, M., Censi, P., Saiano, F., 2013. Simultaneous determinations of zirconium, hafnium, yttrium
734 and lanthanides in seawater according to a co-precipitation technique onto iron-hydroxide. Talanta
735 116, 1085-1090.
736 Roddaz, M., Viers, J., Moreira-Turcq, P., Blondel, C., Sondag, F., Guyot, J.L., et al., 2014. Evidence
737 for the control of the geochemistry of Amazonian floodplain sediments by stratification of suspended
738 sediments in the Amazon. Chemical Geology 387, 101-110.
739 Rouchy, J.M., Caruso, A., 2006. The Messinian salinity crisis in the Mediterranean basin: A
740 reassessment of the data and an integrated scenario. Sedimentary Geology 188-189, 35-67.
741 Rouchy, J.M., Orszag-Sperber, F., Blanc-Valleron, M.M., Pierre, C., Rivière, M., Combourieu-
742 Nebout, N., Panayides, I., 2001. Paleoenvironmental changes at the Messinian-Pliocene boundary in
743 the Eastern Mediterranean (southern Cyprus basins): Significance of the Messinian Lago-Mare.
744 Sedimentary Geology 145, 93-117.
745 Rousseau, T.C.C., Sonke, J.E., Chmeleff, J., Van Beek, P., Souhaut, M., Boaventura, G., Seyler, P.,
746 Jeandel, C., 2015. Rapid neodymium release to marine waters from lithogenic sediments in the
747 Amazon estuary. Nature Communications 6.
748 Schlosser, C., Croot, P.L., 2008. Application of cross-flow filtration for determining the solubility of
749 iron species in open ocean seawater. Limnology and Oceanography: Methods 6, 630-642.
750 Schmidt, K., Bau, M., Hein, J.R., Koschinsky, A., 2014. Fractionation of the geochemical twins Zr-
751 Hf and Nb-Ta during scavenging from seawater by hydrogenetic ferromanganese crusts. Geochimica
752 et Cosmochimica Acta 140, 468-487.
753 Sholkovitz, E., Szymczak, R., 2000. The estuarine chemistry of rare earth elements: Comparison of
754 the Amazon, Fly, Sepik and the Gulf of Papua systems. Earth and Planetary Science Letters 179,
755 299-309.

Sholkovitz, E.R., 1992. Chemical Evolution of Rare-Earth Elements - Fractionation between Colloidal and Solution Phases of Filtered River Water. Earth and Planetary Science Letters 114, 77-84.

Sholkovitz, E.R., 1993. The Geochemistry of Rare-Earth Elements in the Amazon River Estuary. Geochimica et Cosmochimica Acta 57, 2181-2190.

Sholkovitz, E.R., 1995. The aquatic chemistry of rare earth elements in rivers and estuaries. Aquatic Geochemistry 1, 1-34.

Sholkovitz, E.R., Elderfield, H., 1988. Cycling of dissolved rare earth elements in Chesapeake Bay. Global Biogeochemical Cycles 2(2), 157-176.

Sholkovitz, E.R., Landing, W.M., Lewis, B.L., 1994. Ocean Particle Chemistry - the Fractionation of Rare-Earth Elements between Suspended Particles and Seawater. Geochimica et Cosmochimica Acta 58, 1567-1579.

Smith, E., Naidu, R., Alston, A.M., 1999. Chemistry of arsenic in soils: I. Sorption of arsenate and arsenite by four Australian soils. Journal of Environmental Quality 28, 1719-1726.

Stumm, W., 1992. Chemistry of the solid-water interface: processes at the mineral- water and particle-water interface in natural systems. Chemistry of the solid-water interface: processes at the mineral- water and particle-water interface in natural systems.

Taylor, S.R., McLennan, S.M., 1995. The geochemical evolution of the continental crust. Reviews of Geophysics 33, 241-265.

Tepe, N., Bau, M., 2015. Distribution of rare earth elements and other high field strength elements in glacial meltwaters and sediments from the western Greenland Ice Sheet: Evidence for different sources of particles and nanoparticles. Chemical Geology 412, 59-68.

Veyland, A., Dupont, L., Pierrard, J.C., Rimbault, J., Aplincourt, M., 1998. Thermodynamic stability of zirconium(IV) complexes with hydroxy ions. European Journal of Inorganic Chemistry, 1765-1770.

781 Viers, J., Roddaz, M., Filizola, N., Guyot, J.L., Sondag, F., Brunet, P., Zouiten, C., Boucayrand, C.,
782 Martin, F., Boaventura, G.R., 2008. Seasonal and provenance controls on Nd-Sr isotopic
783 compositions of Amazon rivers suspended sediments and implications for Nd and Sr fluxes exported
784 to the Atlantic Ocean. Earth and Planetary Science Letters 274, 511-523.
785 Volkova, A.V., Ermakova, L.E., Golikova, E.V., 2017. Peculiarities of coagulation of the
786 pseudohydrophilic colloids: Aggregate stability of the positively charged gamma-Al2O3 hydrosol in
787 NaCl solutions. Colloids and Surfaces a-Physicochemical and Engineering Aspects 516, 129-138.
788 Wang, L.Y., Lee, M.S., 2016. A review on the aqueous chemistry of Zr(IV) and Hf(IV) and their
789 separation by solvent extraction. Journal of Industrial and Engineering Chemistry 39, 1-9.
790 Xiao, J., He, J., Yang, H., Wu, C., 2017. Comparison between Datangpo-type manganese ores and
791 modern marine ferromanganese oxyhydroxide precipitates based on rare earth elements. Ore Geology
792 Reviews 89, 290-308.
793 Zuddas, P., Censi, P., Inguaggiato, C., Sposito, F., 2018. The behaviour of Zirconium and Hafnium
794 during water-rock interaction. Appl. Geochem. 94, 46-52.
795

FIGURE CAPTIONS

Figure 1 – Geographic sketch map of studied Platani river system illustrating the sampled river portion (in yellow). The enlarged satellite photo shows the Bosco-San Cataldo mine and related landfills.

Figure 2 – Zr vs. Hf linear trends and related slopes calculated for water collected along the streams forming the investigated Platani river system. The high ionic strength river waters are those collected downstream the Bosco S. Cataldo mine.

Figure 3 –A: Zr/Hf vs. ionic strength in DF samples. B: Y/Ho vs. ionic strength in DF samples. C: overall REE concentration vs. ionic strength in DF samples. D: Zr/Hf vs. ionic strength in CF and TDF samples. E: Y/Ho vs. ionic strength in CF and TDF samples. F: overall REE concentration vs. ionic strength in CF and TDF samples. Chondritic Zr/Hf and Y/Ho ratios are reported by Jochum et al. (1986).

Figure 4 – Shale-normalised REE patterns in dissolved fraction of studied river waters relative to PAAS.

Figure 5 - Shale-normalised REE patterns in colloidal (A) and truly dissolved fractions (B) of studied river waters relative to PAAS. Shale-normalised REE patterns of corresponding DF fractions are given for comparison (C).

Figure 6 – A: Scanning electron microscopic image of dolomite nano-sphere aggregates on the Al-bearing substratum from PL-3 sample. B: Particular of the dolomite nanosphere from the abovementioned sample (see spectrum in Fig. 6E). C: Al-bearing substratum (see spectrum in Fig. 6G) and clay mineral microcrysts (see spectrum in Fig. 6F) from sample PL-18. D: Further image of the Al-bearing substratum in sample PL-18 (see spectrum in Fig. 6G). Fe X-ray lines occurring in the reported spectra are probably due to Fe-oxyhydroxide coating of the observed textures. Dashed circles represent the size of x-ray spot for EDS analyses.

820 Figure 7 - Scanning electron microscopic images of colloids from PL-26 water. The distribution of
821 Mg, Al, Si, Ca and Fe is shown in the x-ray maps. In particular, iron is scattered on the whole surface
822 of the colloid, suggesting its occurrence as encrustation of the colloidal surface.
823 Figure 8 - X-ray diffraction patterns (Ni-filtered CuKα radiation, scan speed 1° min^{-1}) illustrating the
824 minerals occurring in fine (< 2 μm) and coarse (> 2 μm) sediment fractions collected from the most
825 representative studied sites.
826 Figure 9 – A: X-ray diffraction of suspended particulate matter collected from PL-5 water sample.
827 The diffraction effects of kaolinite, quartz, calcite and dolomite are shown. B: X-ray diffraction of
828 suspended particulate matter collected from PL-37 water sample. C: SEM images of suspended
829 particulate matter (> 450 nm) from PL-5 water. The coherent distribution of Al and Si reported in
830 related x-ray maps suggests the distribution of clay minerals representing the finest fraction of
831 suspended solids occurring in the background of the SEM image. Areas where Al accumulation
832 occurs relative to Si, probably indicate the occurrence of Al-oxyhydroxides (see the red dashed
833 rectangular area in Al map). Ca, Mg and S maps show that carbonates and gypsum crystals and rock
834 fragments form the coarse fraction of the suspended solids.
835 Figure 10 - Zr vs. Hf values analysed in fractions extracted from studied river sediments. The
836 reported equation represents the linear regression calculated on all the reported analyses.
837 Figure 11 – Shale-normalised REE patterns relative to Post Archean Australian Shale (PAAS)
838 calculated in fractions extracted from river sediments. Features of REE patterns are summarised in
839 terms of HREE/LREE fractionation and extent of MREE enrichment calculated as in Fig. 5. REE
840 analyses of Marls, Evaporitic limestone, Dolostone and Laminar gypsum are average values and are
841 reported in Table S7 of the supplementary on-line material.
842 Figure 12 – Change of Zr/Hf ratio in CF with pH.
843 Figure 13 – (A): Zr/Hf vs. [REE] in dissolved fraction (DF) of studied river waters. The hypothetical
844 end-members of the observed hyperbolic distribution are also indicated as EM-1 and EM-2. The

composition of colloids (CF) and truly dissolved fraction (TDF) extracted from selected river waters and high ionic strength waters are also reported. (B): Companion plot illustrating the linear relationship occurring between 1/[REE] vs. Zr/Hf ratio in studied DF samples depicted to confirm that the hyperbola in Fig. 9A really represents a mixing path (Langmuir et al., 1978). Chondritic Zr/Hf and Y/Ho ratios are reported by Jochum et al. (1986).

Figure 14 – Changes of REE, Al and Fe concentrations in DF with ionic strength.

Figure 15 – A: Zr/Hf values in the 1^{st} sediment fraction reported vs. pH. B: Zr/Hf values of the 1^{st} sediment fraction reported vs. saturation index of dolomite assessed in coexisting river waters. C: Zr/Hf values in the 2^{nd} sediment fraction reported vs. pH. D: Zr/Hf values in the 3^{rd} sediment fraction reported vs. pH. Chondritic Zr/Hf ratios are reported by Jochum et al. (1986).

TABLE CAPTIONS

Table 1 – Overall REE concentration, ionic strength, Y/Ho, Zr/Hf, Ce/Ce* and Gd/Gd* values measured in studied aqueous samples (DF, CF and TDF) and in extracted sediment fractions. The related error values (Δ_i) values are also given. Features of the shale normalised REE pattern for each sample are also reported in terms of HREE/LREE fractionation and extent of MREE enrichment (MREE/MREE*).

Table

DF	μ	∑[REE]	Y/Ho	$\Delta_{Y/Ho}$	Zr/Hf	$\Delta_{Zr/Hf}$	Ce/Ce*	Δ_{CeCe*}	Gd/Gd*	$\Delta_{Gd/Gd*}$	HREE/L REE	MREE/ MREE*
	mol kg^{-1}	nmol kg^{-1}			molar ratio							
PL-1	0.47	1.02	54.5	0.21	249.8	0.2	1.2	0.5	1.0	0.5	1.6	1.7
PL-2	0.34	1.62	53.4	0.19	105.2	0.6	0.7	0.5	1.0	0.4	0.7	1.1
PL-3	3.83	1.75	90.0	0.15	321.3	0.4	1.1	0.5	1.3	0.5	4.0	0.9
PL-4	0.51	1.57	59.3	0.21	100.2	0.4	0.6	0.5	0.8	0.5	0.7	0.9
PL-5	3.22	1.60	73.2	0.13	350.4	0.5	1.4	0.5	1.2	0.4	5.4	1.0
PL-6	1.77	0.80	81.2	0.23	258.3	1.2	1.2	0.7	1.2	0.6	3.1	1.2
PL-7	5.15	1.74	71.5	0.09	285.0	0.5	1.2	0.3	1.0	0.3	4.7	1.1
PL-8	0.56	0.64	61.2	0.17	112.0	1.5	1.1	0.5	1.7	0.5	5.6	0.9
PL-9	0.80	1.13	60.4	0.12	92.1	0.7	0.9	0.3	3.9	0.3	3.0	2.0
PL-10	0.71	0.48	66.6	0.20	180.1	2.0	1.1	0.8	2.3	0.7	11.9	0.7
PL-11	1.89	1.11	69.0	0.12	104.5	0.9	1.0	0.3	2.9	0.3	3.2	1.8
PL-12	0.51	3.10	54.2	0.06	86.7	0.4	0.9	0.1	1.1	0.1	1.2	1.7
PL-13	0.88	4.95	40.8	0.03	76.7	0.1	0.9	0.1	1.0	0.1	1.8	1.6
PL-15	0.11	0.82	61.2	0.15	120.4	0.8	1.1	0.4	1.4	0.1	4.4	1.3
PL-16	0.31	1.32	57.5	0.11	90.8	0.4	1.1	0.3	1.0	0.4	2.1	1.8
PL-17	0.13	5.37	52.9	0.03	54.7	0.1	1.1	0.1	1.0	0.3	1.5	2.2
PL-18	0.31	0.99	65.0	0.15	135.1	0.4	1.1	0.4	1.7	0.1	5.0	1.2
PL-19	1.07	0.93	53.4	0.18	74.6	0.6	1.0	0.4	6.5	0.4	2.4	3.3
PL-20	0.68	2.72	38.7	0.05	63.5	0.2	1.0	0.1	1.0	0.3	2.0	2.0
PL-21	0.65	1.48	38.1	0.08	79.9	0.4	0.9	0.2	1.0	0.1	2.6	1.7
PL-22	0.19	0.31	42.4	0.21	212.1	5.6	0.9	1.0	3.8	0.2	20.6	0.5
PL-23	0.19	2.22	44.8	0.05	62.1	0.5	1.0	0.1	1.5	0.9	2.8	1.6
PL-24	0.22	0.85	25.3	0.09	54.8	0.6	0.9	0.2	0.9	0.1	5.5	1.7
PL-25	0.36	1.04	60.0	0.16	133.0	1.2	1.0	0.4	1.4	0.2	2.0	1.5
PL-26	0.30	0.76	49.0	0.27	138.7	0.7	1.1	0.8	2.7	0.3	3.3	1.1
PL-27	0.38	3.76	47.0	0.03	58.0	0.3	1.1	0.1	1.1	0.7	1.9	2.0
PL-28	0.57	49.16	47.0	0.00	55.0	0.0	1.1	0.0	0.9	0.1	1.4	2.5
PL-29	0.45	28.18	42.5	0.00	50.3	0.0	1.1	0.0	0.9	0.0	1.4	2.6
PL-30	0.23	16.75	43.0	0.01	51.0	0.1	1.1	0.0	1.0	0.0	1.5	2.4
PL-31	0.27	2.10	42.0	0.05	67.2	0.8	0.9	0.1	0.8	0.0	2.2	2.3
PL-32	0.15	27.39	44.9	0.00	57.3	0.1	1.1	0.0	0.9	0.1	1.4	2.4
PL-33	0.25	3.29	52.8	0.04	60.3	0.4	1.0	0.1	1.2	0.0	1.9	1.9
PL-34	0.32	5.19	55.0	0.03	56.3	0.2	1.0	0.1	1.1	0.1	1.7	2.0
PL-35	0.29	3.29	54.8	0.04	50.3	0.2	1.0	0.1	1.1	0.1	1.9	1.9
PL-36	0.33	6.00	54.5	0.02	53.9	0.1	1.1	0.0	1.1	0.1	1.6	2.1
PL-37	0.28	7.32	55.2	0.02	57.0	0.1	1.1	0.0	1.0	0.0	1.5	2.1
PL-38	0.29	9.65	55.8	0.02	56.6	0.1	0.9	0.0	1.1	0.0	1.3	1.9

CF	μ	∑[REE]	Y/Ho	$\Delta_{Y/Ho}$	Zr/Hf	$\Delta_{Zr/Hf}$	Ce/Ce*	Δ_{CeCe*}	Gd/Gd*	$\Delta_{Gd/Gd*}$	HREE/L REE	MREE/ MREE*
	mol kg^{-1}	pmol kg^{-1}			molar ratio							
PL-1	0.47	0.61	52.0	0.31	234.8	0.8	0.8	0.0	1.0	0.1	1.8	1.5
PL-3	3.83	0.11	39.8	0.04	497.3	0.4	2.5	0.0	1.1	0.0	2.2	0.6
PL-5	3.22	0.25	36.3	0.05	396.7	0.3	2.1	0.0	1.4	0.0	3.6	0.8
PL-8	0.56	0.39	49.7	0.11	164.9	2.5	0.6	0.0	1.6	0.0	4.6	0.9
PL-10	0.11	0.12	24.6	0.07	525.4	4.8	1.5	0.0	3.4	0.0	8.8	0.6
PL-15	0.31	0.58	59.5	0.11	82.3	1.6	0.9	0.1		0.1	5.0	1.3
PL-18	0.19	0.51	60.7	0.08	146.1	0.4	0.9	0.1	1.7	0.1	5.1	1.0
PL-26	0.30	0.81	63.1	0.24	199.6	1.4	0.6	0.1	3.0	0.1	5.9	1.0

TDF	μ	∑[REE]	Y/Ho	$\Delta_{Y/Ho}$	Zr/Hf	$\Delta_{Zr/Hf}$	Ce/Ce*	Δ_{CeCe*}	Gd/Gd*	$\Delta_{Gd/Gd*}$	HREE/L REE	MREE/ MREE*
	mol Kg^{-1}	nmol kg^{-1}			molar ratio							
PL-1	0.47	0.02	37.1	0.31	275.9	1.3	1.1	2.2	1.3	9.4	6.3	0.9
PL-3	3.83	0.59	105.3	0.04	154.6	0.5	1.1	0.1	1.3	0.6	4.1	0.9
PL-5	3.22	0.39	100.4	0.05	172.2	1.5	0.9	0.2	1.1	0.8	7.3	0.8
PL-8	0.56	0.14	90.4	0.11	80.2	1.9	0.7	0.9	2.2	2.3	18.5	0.5
PL-10	0.11	0.23	87.5	0.07	92.0	1.8	0.6	0.5	1.6	1.2	15.8	0.6
PL-15	0.31	0.03	46.7	0.11	142.8	0.8	0.9	1.5	2.7	10.8	3.0	1.1
PL-18	0.19	0.06	55.9	0.08	86.1	1.9	1.0	0.7	1.6	4.6	4.1	1.1
PL-26	0.30	0.08	64.2	0.24	66.5	2.1	1.0	0.6	1.9	3.3	4.6	1.2

1st sediment fraction	∑[REE]	Y/Ho	$\Delta_{Y/Ho}$	Zr/Hf	$\Delta_{Zr/Hf}$	Ce/Ce*	Δ_{CeCe*}	Gd/Gd*	$\Delta_{Gd/Gd*}$	HREE/L REE	MREE/ MREE*
	nmol kg^{-1}			molar ratio							
PL-1	40.7	68.1	0.00	43.8	0.34	0.9	0.01	1.0	0.0	1.2	2.2
PL-3	28.8	62.7	0.01	117.7	0.90	0.8	0.01	1.0	0.0	0.9	2.4
PL-5	27.5	67.3	0.01	87.3	0.61	0.8	0.01	1.0	0.0	0.9	2.5
PL-8	37.0	65.8	0.00	87.0	0.73	0.8	0.01	1.0	0.0	0.9	2.6
PL-10	37.6	67.8	0.00	96.2	0.86	0.8	0.01	0.9	0.0	0.9	2.2
PL-18	37.4	66.3	0.00	43.5	0.73	0.8	0.01	0.9	0.0	1.1	2.2
PL-26	41.8	70.5	0.00	44.8	0.57	0.8	0.01	1.0	0.0	1.0	2.6

2nd sediment fraction	∑[REE]	Y/Ho	$\Delta_{Y/Ho}$	Zr/Hf	$\Delta_{Zr/Hf}$	Ce/Ce*	Δ_{CeCe*}	Gd/Gd*	$\Delta_{Gd/Gd*}$	HREE/L REE	MREE/ MREE*
	nmol kg^{-1}			molar ratio							
PL-1	1.8	59.3	0.05	92.7	5.88	1.0	0.27	0.9	0.1	2.8	2.2
PL-3	5.8	72.1	0.02	94.4	2.05	1.1	0.07	0.9	0.1	2.3	2.3
PL-5	5.8	76.0	0.02	117.5	1.64	0.9	0.06	1.0	0.1	1.5	2.0
PL-8	4.5	73.9	0.03	170.9	2.04	0.9	0.08	1.0	0.1	1.6	2.4
PL-10	5.8	82.7	0.02	159.3	4.09	0.9	0.06	1.0	0.1	1.5	2.3
PL-18	5.8	97.8	0.03	127.6	10.61	0.9	0.05	0.9	0.1	1.5	2.2
PL-26	4.4	90.9	0.04	114.4	2.70	0.9	0.08	1.1	0.1	1.1	2.2

3rd sediment fraction	∑[REE]	Y/Ho	$\Delta_{Y/Ho}$	Zr/Hf	$\Delta_{Zr/Hf}$	Ce/Ce*	Δ_{CeCe*}	Gd/Gd*	$\Delta_{Gd/Gd*}$	HREE/L REE	MREE/ MREE*
	nmol kg^{-1}			molar ratio							
PL-1	13.0	48.7	0.01	65.0	0.02	1.1	0.03	1.0	0.0	1.5	2.1
PL-3	20.1	46.7	0.01	57.1	0.01	1.0	0.02	0.9	0.0	1.3	2.2
PL-5	22.9	47.1	0.01	58.6	0.01	1.0	0.01	0.9	0.0	1.3	2.2
PL-8	19.0	47.1	0.01	51.1	0.01	0.9	0.02	0.9	0.0	1.3	2.5
PL-10	7.1	47.6	0.01	75.4	0.04	1.2	0.05	0.8	0.0	2.0	1.9
PL-18	21.6	46.6	0.01	58.6	0.02	1.1	0.02	0.9	0.1	1.8	2.2
PL-26	3.6	51.9	0.03	86.1	0.11	1.0	0.10	0.8	0.0	1.4	2.5

4th sediment fraction	∑[REE]	Y/Ho	$\Delta_{Y/Ho}$	Zr/Hf	$\Delta_{Zr/Hf}$	Ce/Ce*	Δ_{CeCe*}	Gd/Gd*	$\Delta_{Gd/Gd*}$	HREE/L REE	MREE/ MREE*
	nmol kg^{-1}			molar ratio							
PL-1	26.3	23.4	0.01	79.9	0.00	2.1	0.01	1.7	0.0	1.9	2.9
PL-3	19.8	58.7	0.01	75.1	0.00	1.5	0.01	0.8	0.0	1.4	1.7
PL-5	23.7	49.7	0.00	75.0	0.00	1.5	0.02	0.9	0.0	2.1	1.7
PL-8	27.9	42.4	0.01	76.3	0.00	2.1	0.01	1.5	0.0	1.2	1.6
PL-10	533.8	34.4	0.00	75.2	0.00	1.1	0.00	1.1	0.0	1.1	1.6
PL-18	136.0	39.7	0.00	76.2	0.00	1.8	0.00	0.9	0.0	1.4	1.6
PL-26	43.1	32.8	0.00	71.6	0.00	1.5	0.01	0.8	0.0	1.1	1.4

Figure


Sicily
Palermo
Appennino-Maghrebide range
Platani river
Bosco-S. Cataldo mine
N
Iblean plateau
Main outcrops of Messinian evaporites in Sicily
landfill of Kainite mine
Bosco-S. Cataldo mine (abandoned)
landfill of sulphur mine
Streams belonging to the Platani catchment

Fig. 1

Figure

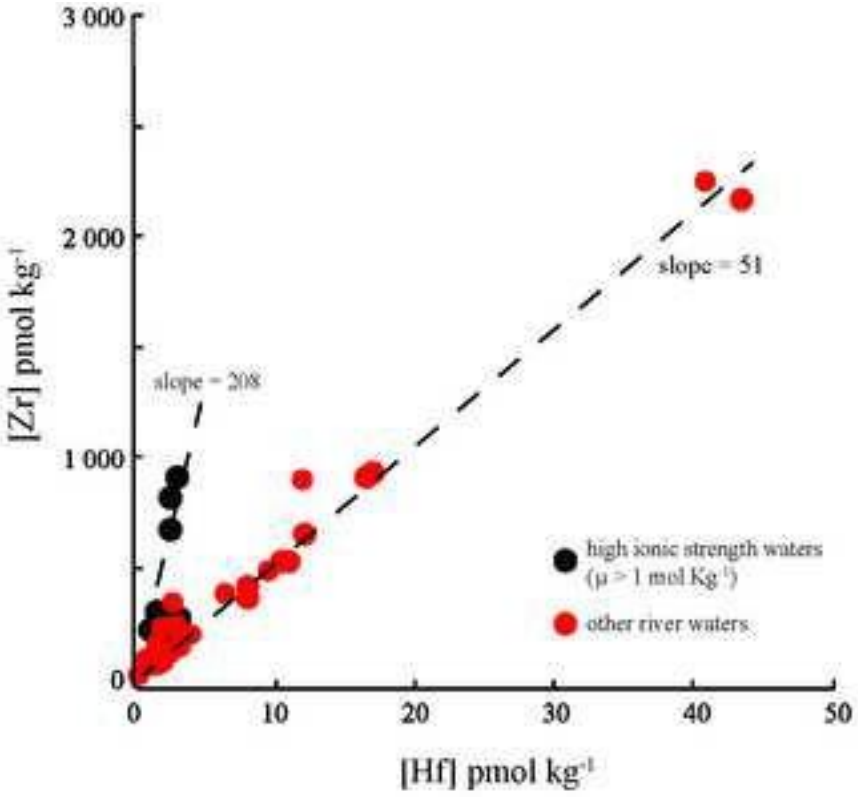
3 000
2 000
1 000
0
[Zr] pmol kg-1
0
10
20
30
40
50
[Hf] pmol kg-1
slope = 208
slope = 51
high ionic strength waters
(μ > 1 mol Kg-1)
other river waters

Fig. 2

Figure

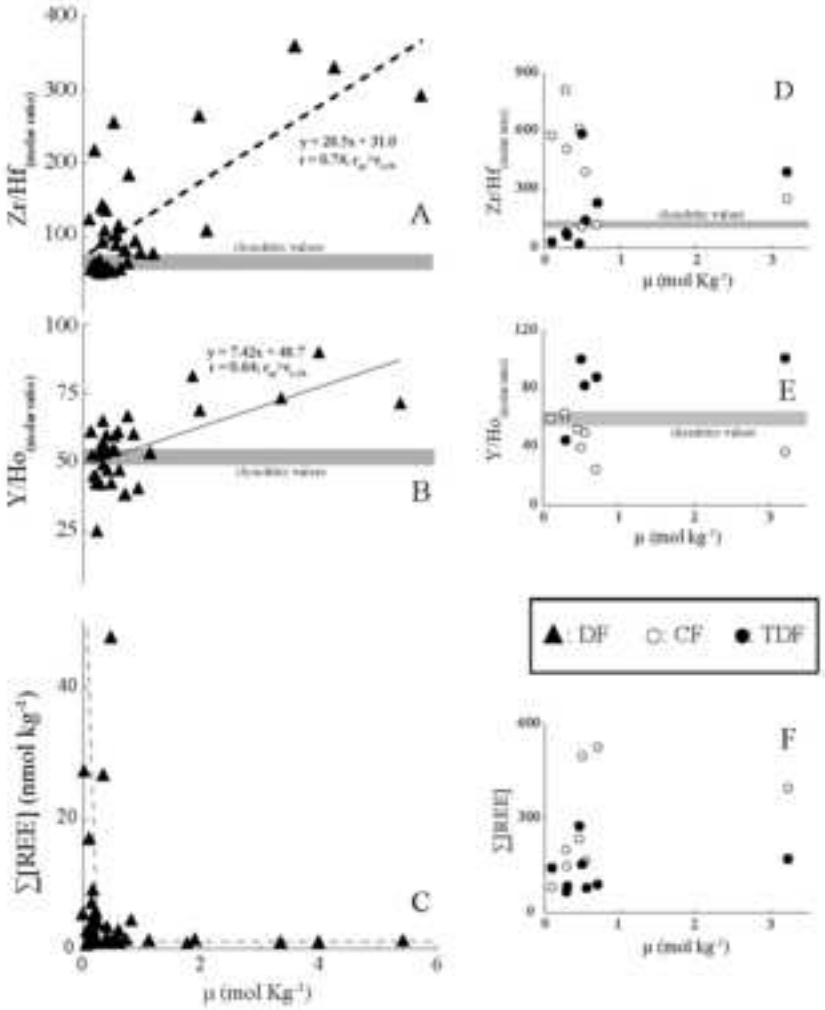

Fig. 3

Figure

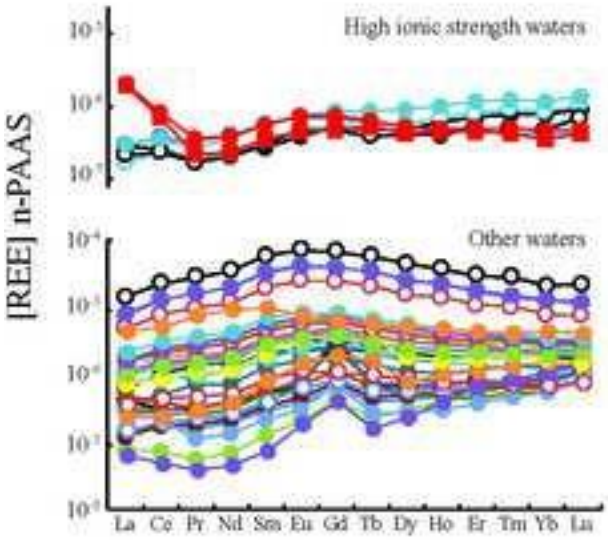
High ionic strength waters
Other waters
[REE] n-PAAS
La Ce Pr Nd Sm Eu Gd Tb Dy Ho Er Tm Yb Lu

Fig. 4

Figure

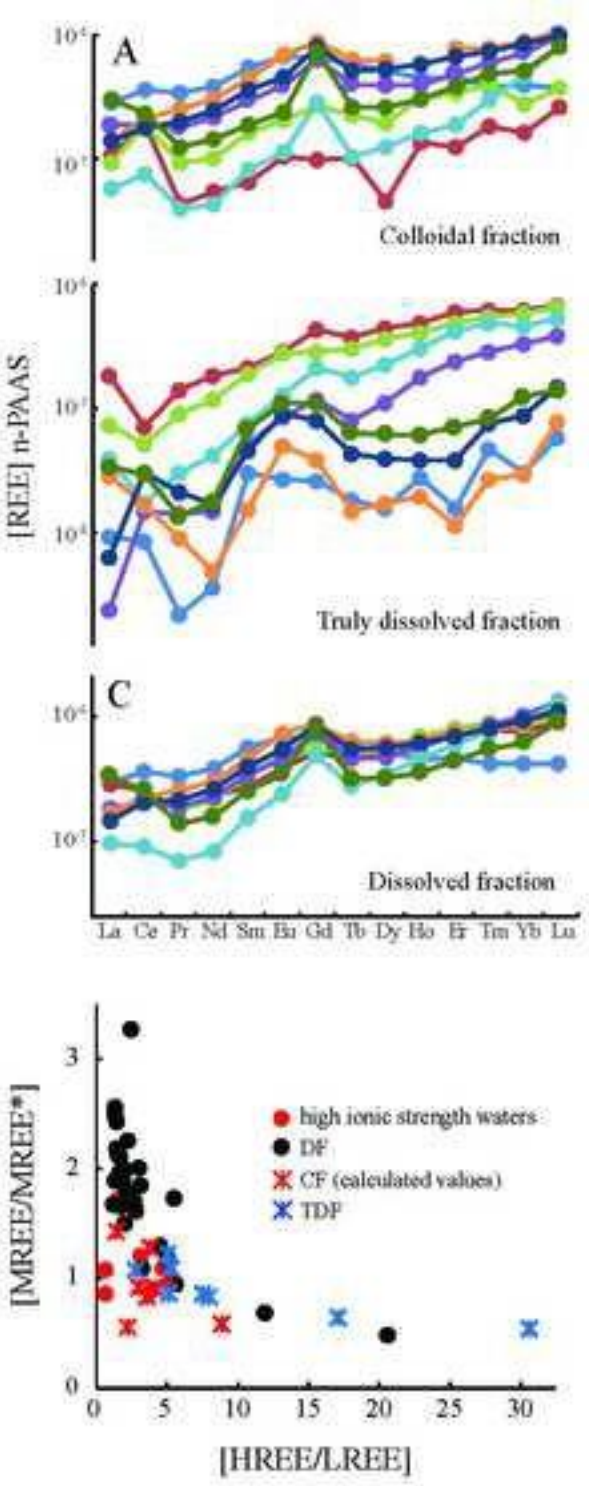
A
Colloidal fraction
[REE] n-PAAS
Truly dissolved fraction
C
Dissolved fraction
La Ce Pr Nd Sm Eu Gd Tb Dy Ho Er Tm Yb Lu
[MREE/MREE*]
high ionic strength waters
DF
CF (calculated values)
TDF
[HREE/LREE]

Fig. 5

Figure

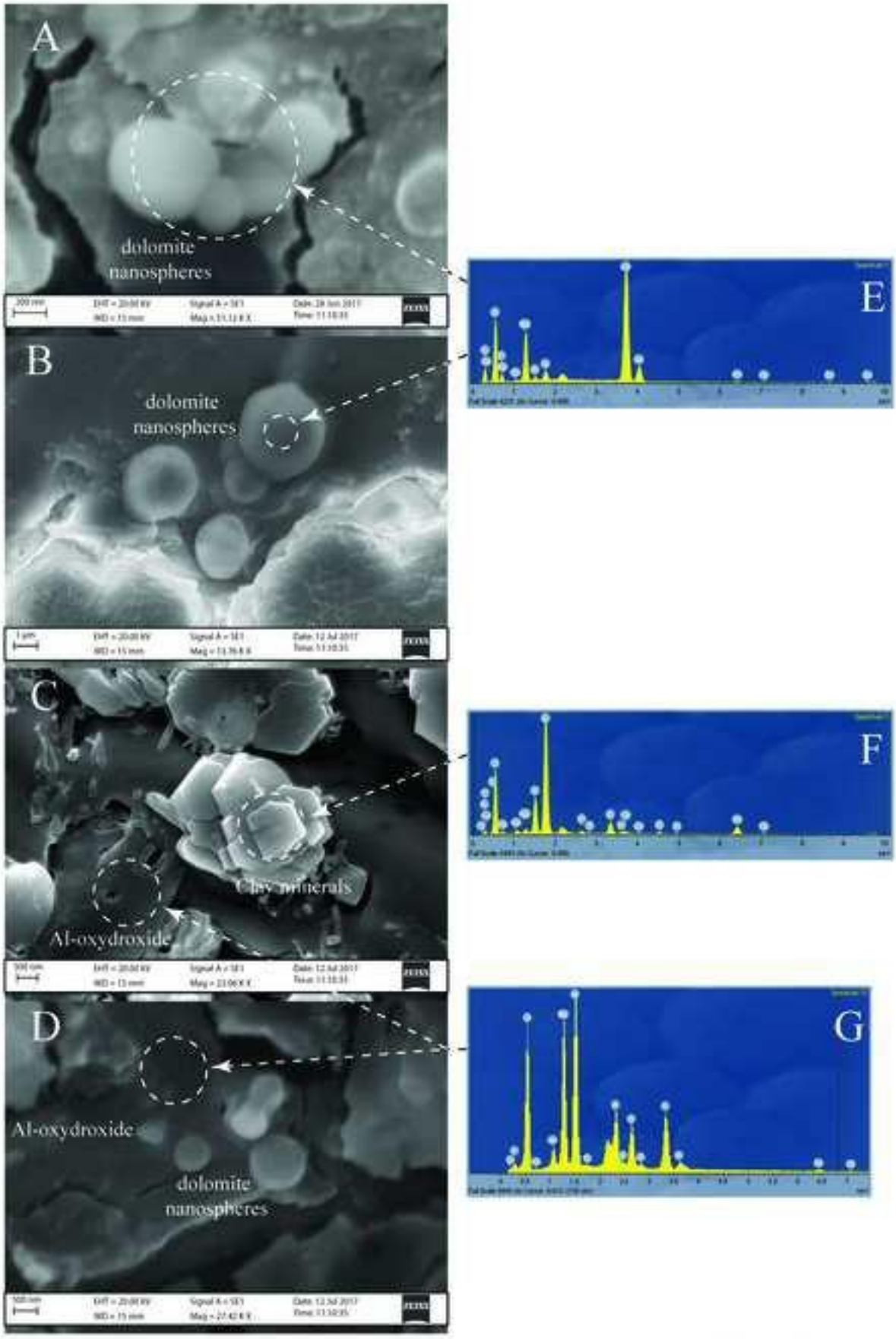
A
dolomite
nanospheres
B
dolomite
nanospheres
C
Clay minerals
Al-oxydroxide
D
Al-oxydroxide
dolomite
nanospheres
E
F
G

Fig. 6

Figure

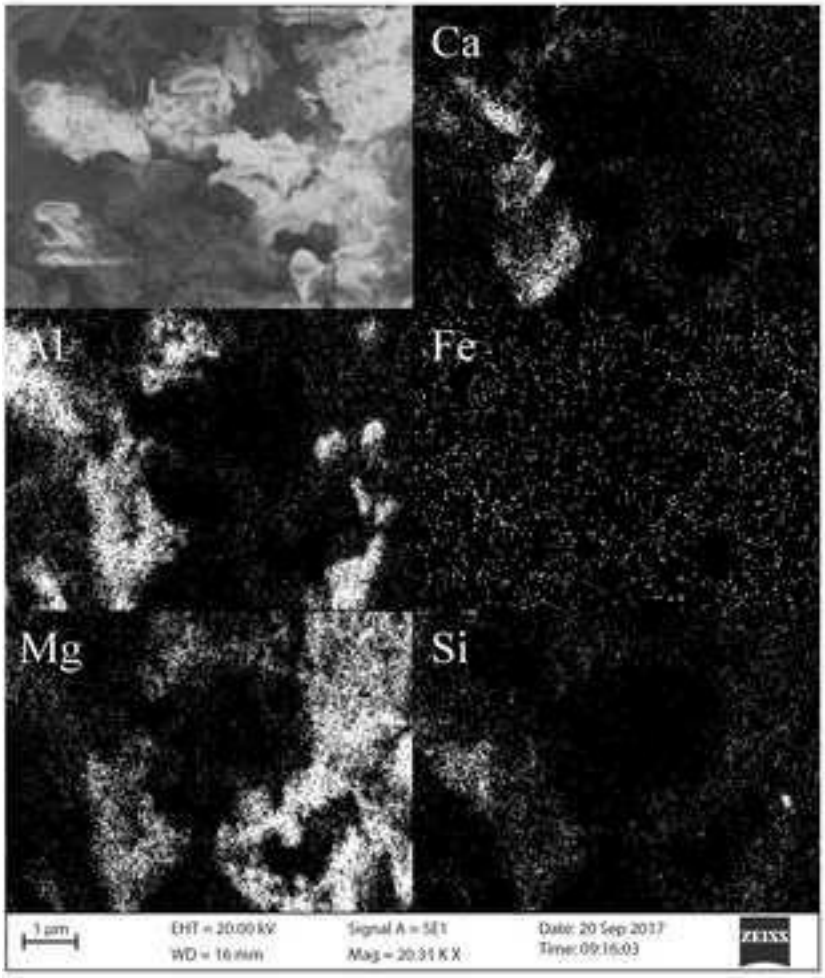
Ca
Al
Fe
Mg
Si
1 µm
EHT = 20.00 kV
WD = 16 mm
Signal A = SE1
Mag = 20.31 K X
Date: 20 Sep 2017
Time: 09:16:03
ZEISS

Fig. 7

Figure

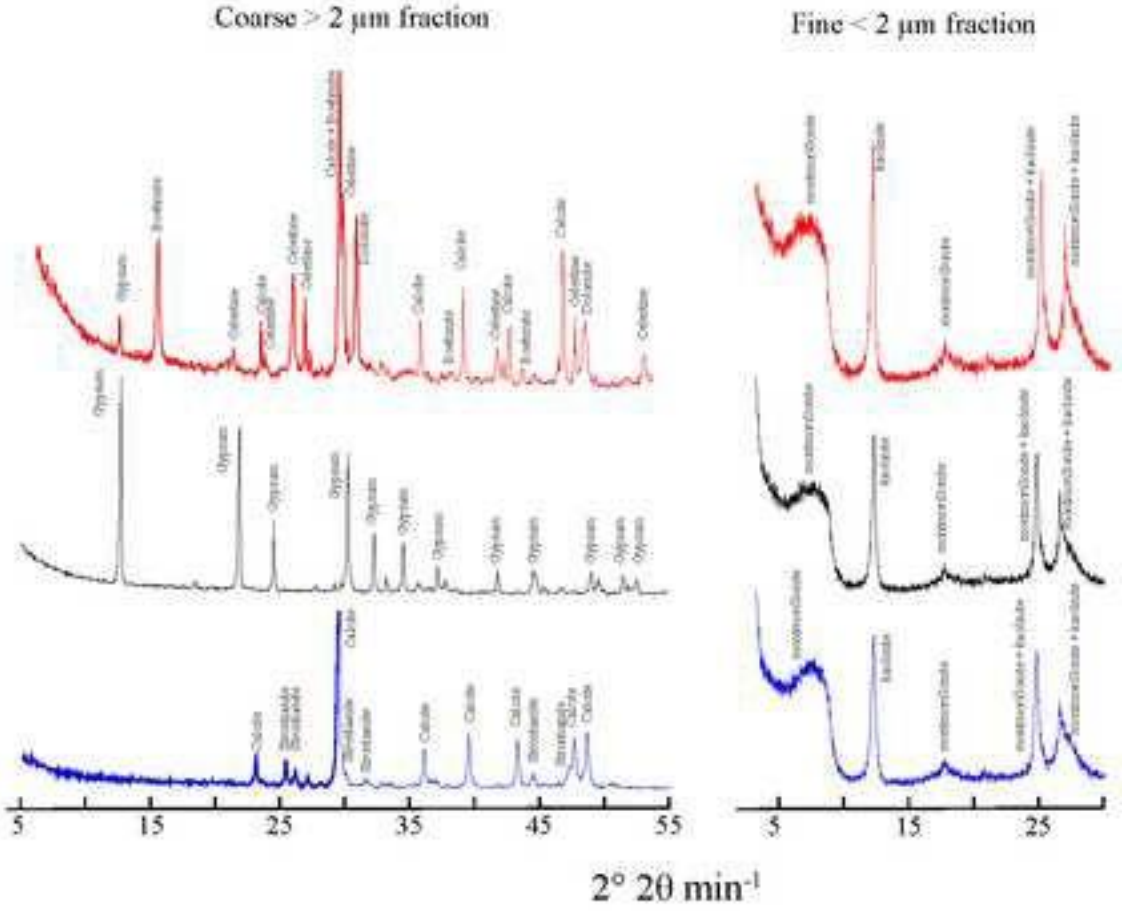
Coarse > 2 µm fraction
Fine < 2 µm fraction
5
15
25
35
45
55
5
15
25
2° 2θ min-1

Fig. 8

Figure

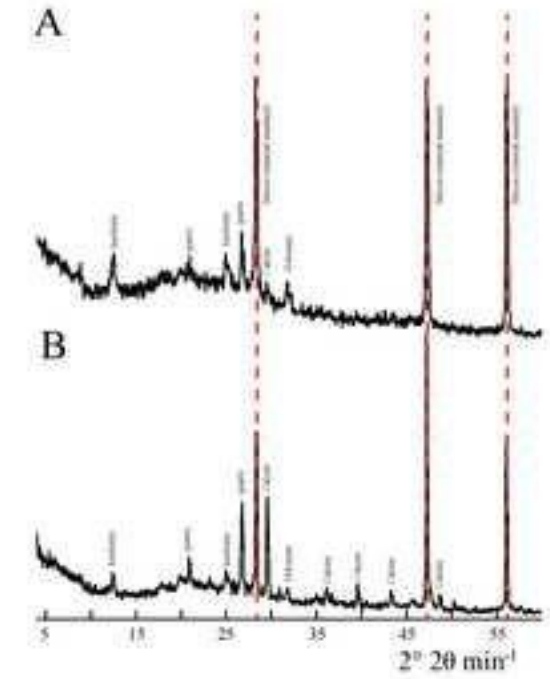

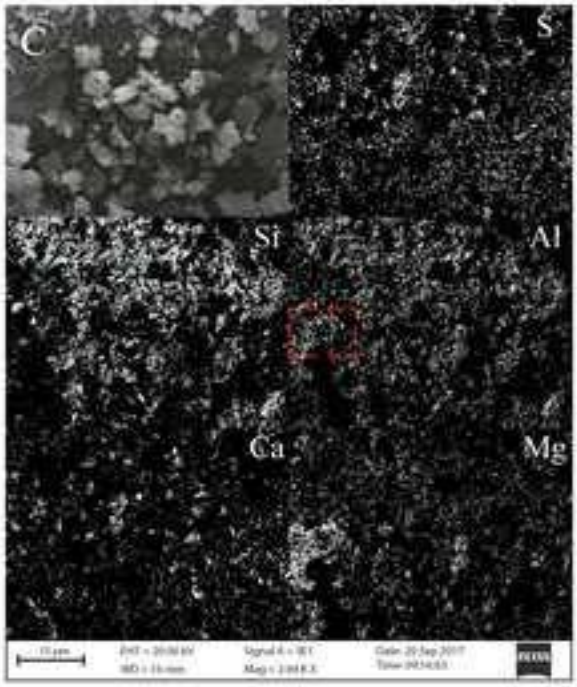

Fig. 9

Figure

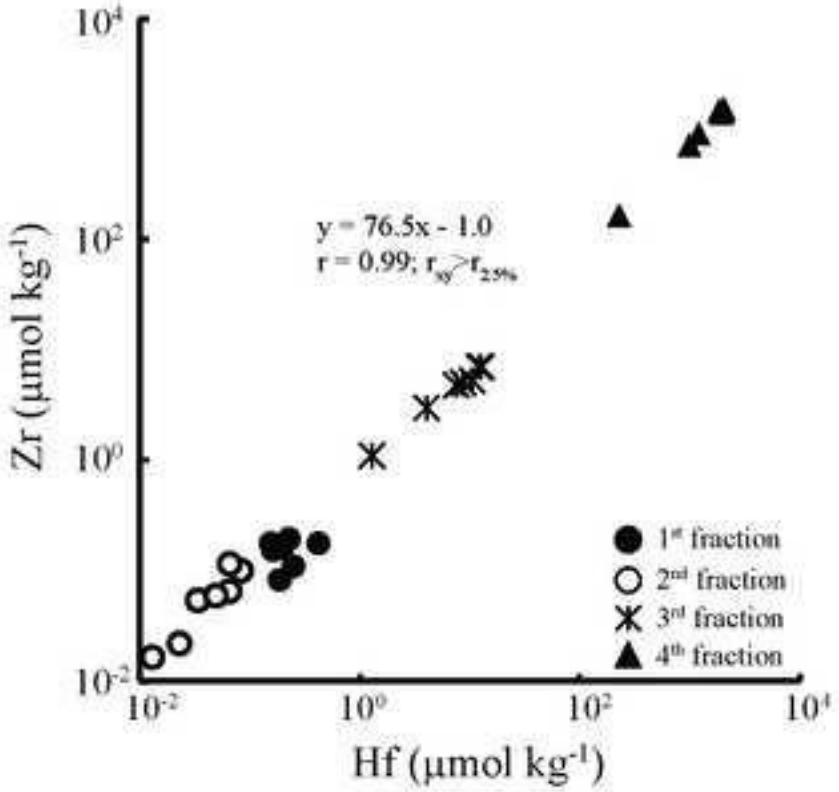

Fig. 10

Figure

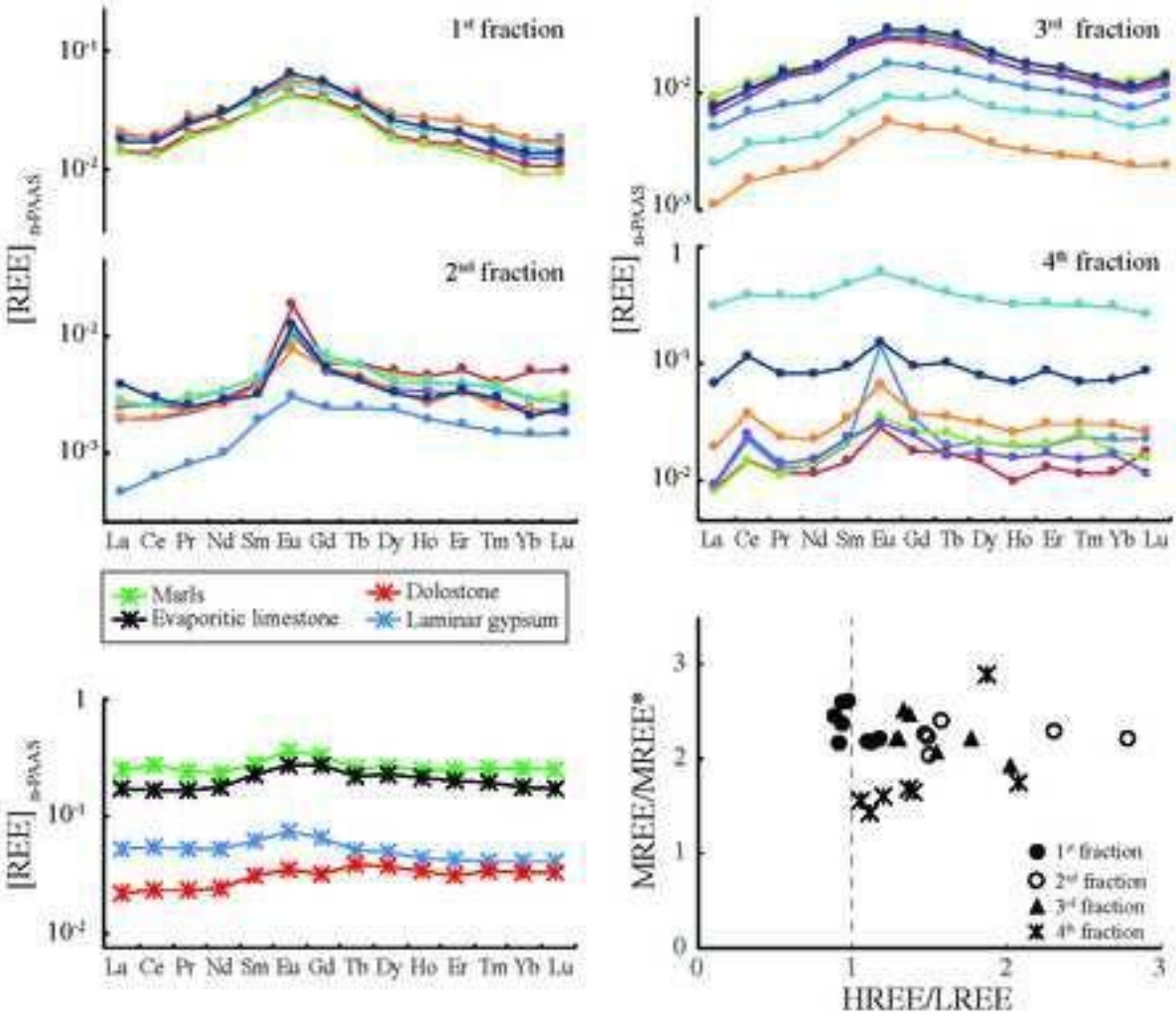

Fig. 11

Figure

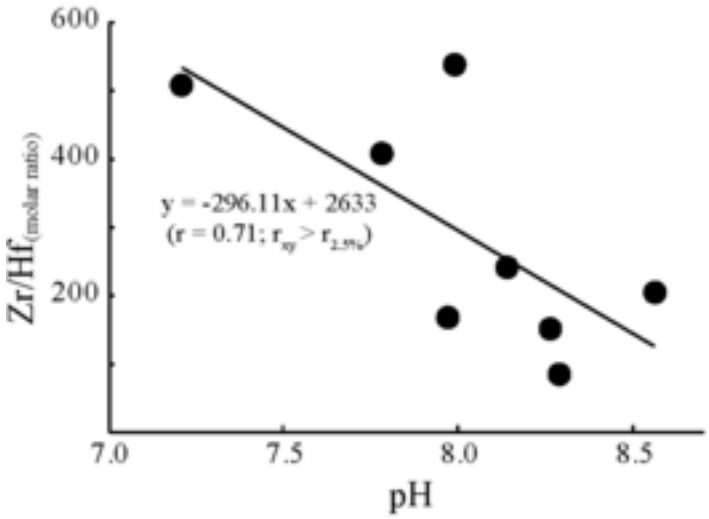

Fig. 12

Figure

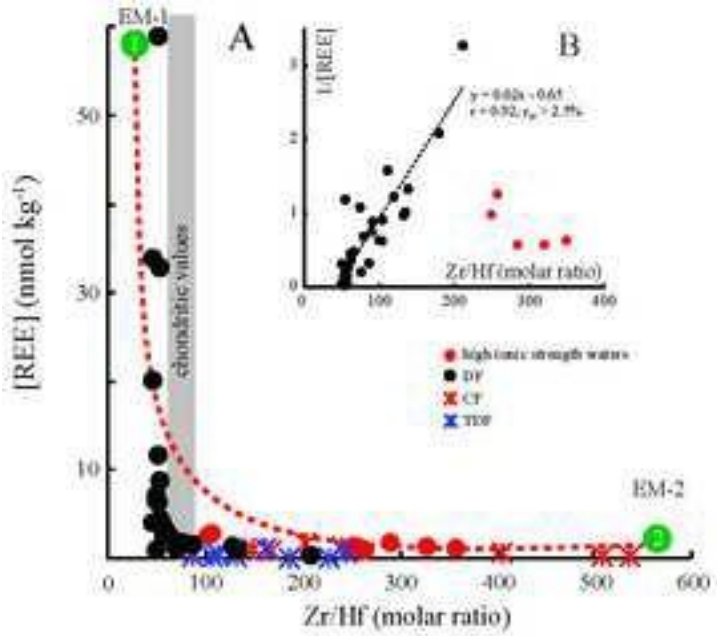

Fig. 13

Figure

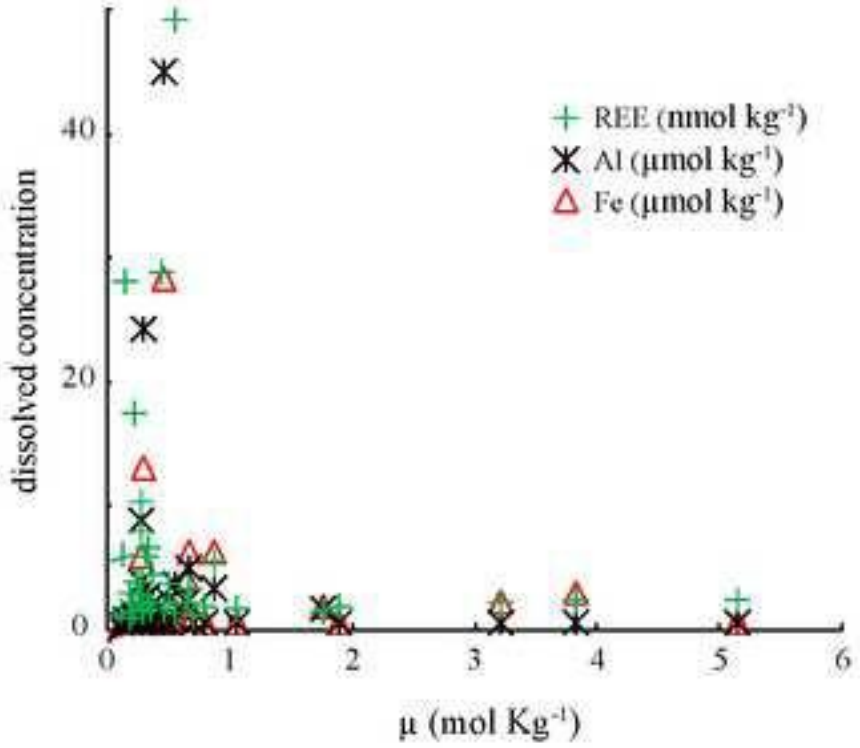

Fig. 14

Figure

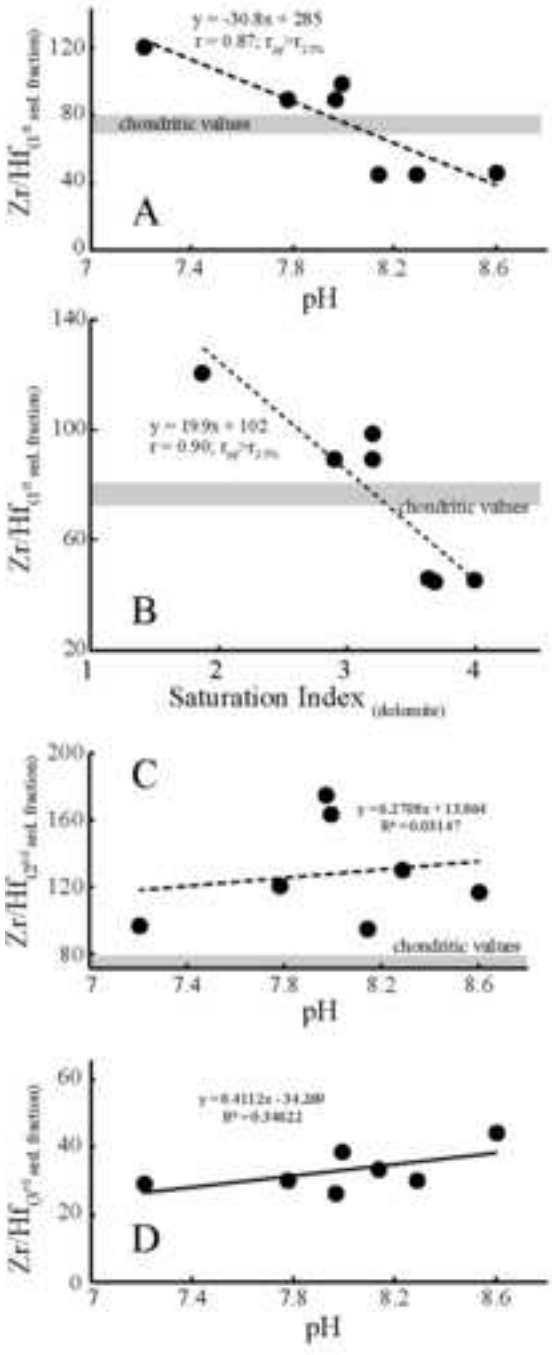

Fig. 15